Orogeny and orography: The effects of erosion on the structure of mountain belts

Sean D. Willett[1]

Department of Geosciences, Pennsylvania State
University, University Park

Abstract. A numerical model of the coupled processes of tectonic deformation and surface erosion in convergent orogens is developed to investigate the nature of the interaction between these processes. Crustal deformation is calculated by a two-dimensional finite element model of deformation in response to subduction and accretion of continental crust. Erosion operates on the uplifted surface of this model through fluvial incision which is taken to be proportional to stream power. The relative importance of the tectonic and erosion processes is given by a dimensionless "erosion number" relating convergence velocity, rock erodibility, and precipitation rate. This number determines the time required for a system to reach steady state and the final topographic shape and size of a mountain belt. Fundamental characteristics of the model orogens include asymmetric topography with shallower slopes facing the subducting plate and an asymmetric pattern of exhumation with the deepest levels of exhumation opposite to subduction. These characteristics are modified when the regional climate exhibits a dominant wind direction and orographically enhanced precipitation on one side of the mountain belt. The two possible cases are dominant wind in the direction of motion of the subducting plate and dominant wind direction in the opposite direction of the subducting plate velocity. Models of the former case predict a broad zone of exhumation with maximum exhumation in the orogen interior. Models of the latter case predict a focused zone of exhumation at the margin of the orogen and, at high erosion number, a reversal in the topographic asymmetry. Natural examples of these two cases are presented. The Southern Alps of New Zealand exhibits the climate and exhumation asymmetry characteristic of wind in the direction opposite to motion of the subducting plate. The asymmetry of topography suggests that erosion is not efficient enough to have reversed the topographic asymmetry. The contrasting example of dominant wind in the direction of subduction motion is provided by the Olympic Mountains of Washington State. In this case, exhumation of deep levels of the Cascadia accretionary wedge shows a broad domal pattern consistent with the observed orographic precipitation.

1. Introduction

Surface processes and erosion play an important role in modifying the geologic expression of orogenic processes. Convergent orogens exhibit the highest rates of surface uplift on Earth, and it is not surprising that they are also the site for the highest rates of erosion. Erosion is frequently the principal mechanism for exhuming deeper levels of a convergent orogenic belt, thereby providing the surface exposure of metamorphism at depth. In addition, erosion modifies or even destroys the excess topography of a mountain belt, thereby modifying the size, form, and internal deformation of an orogen. Deformation, surface uplift, and erosion comprise a system with feedback in which deformation leads to surface uplift, but surface uplift leads to an increase in erosion through orographic enhancement of precipitation (Figure 1). Mountain topography in convergent orogens is thus the result of the balance between tectonic uplift and uplift-enhanced precipitation and erosion.

There are two primary mechanisms by which erosional feedback affects deformation in orogenic belts. First is the influence on mass balance between material accreted by convergence and material lost by erosion and subsequently removed from the orogenic system. Given the climatic feedback between surface uplift and erosion rates, it is possible that small orogenic belts with high erosion rates reach a steady state in which erosional mass flux out of a system balances accretionary flux into the system. This has been proposed for a number of orogens including the arc-continent collision in Taiwan [*Suppe*, 1980, 1981; *Barr and Dahlen*, 1989; *Barr et al.*, 1991], for the Southern Alps of New Zealand [*Adams*, 1980; *Norris et al.*, 1990; *Koons*, 1989] and for the Cascadia forearc high in the Olympic Peninsula [*Brandon et al.*, 1998]. Even if these small orogenic belts are not in a steady state, it is clear that erosion has strongly affected their size and structure.

The second mechanism by which erosion affects crustal deformation is through perturbations to the gravitational stresses within the orogen. Modern models of the mechanical processes of orogenesis are strongly rooted in the concepts of critical form proposed by *Chapple* [1978] and extensively developed by *Davis et al.* [1983], *Dahlen* [1984, 1990] and others. Although these critical wedge models were originally developed for application to accretionary wedges and fold-and-thrust belts, it has been recognized that they also apply to orogenic belts at a larger scale [*Jamieson and Beaumont*,
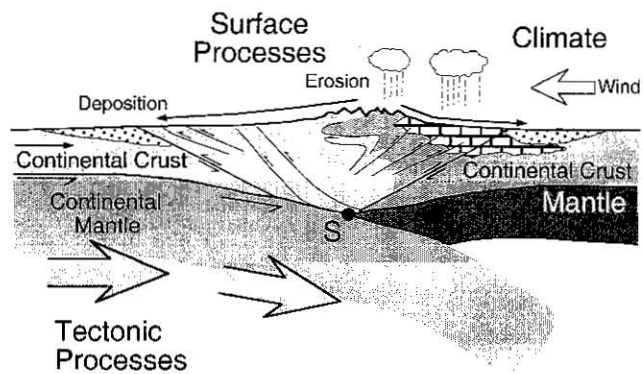
Figure 1. Conceptual view of the feedbacks inherent to the tectonic, surficial, and climatic processes in orogenesis. Convergence leads to crustal thickening and isostatic uplift. Increased elevation perturbs local climate, increasing precipitation and increasing erosion.

1988; *Willett et al.*, 1993]. In a critical wedge model the large-scale topographic shape of an orogenic belt reflects a balance between gravitational stresses arising from the surface slope and basal shear stresses resulting from underthrusting of stronger material beneath the wedge. Surface slopes, and hence excess topography, develop to increase stresses to the point that material throughout the wedge is at the point of plastic failure. Continued accretion induces deformation throughout the wedge, leading to self-similar growth, that is, an increase in the size of the wedge without a change in the cross-sectional shape. The concepts of suborogen subduction, critical shape, and self-similar growth also apply at larger scales. At the scale of an orogenic belt, the deforming domain does not take the simple form of a wedge but has a sectional shape that reflects the strength and physical properties of the entire deforming crust. Initially, this might take the form of back-to-back doubly-vergent wedges, but larger orogens representing greater convergence reach a maximum elevation and form high, interior plateaus [*Willett and Beaumont*, 1994; *Royden*, 1996]. However, the principle of a critical topographic form or the entire orogen still holds even at this largest scale.

Surface processes that perturb the critical topographic form will have an effect on the internal stresses and the distribution of deformation. If surface processes redistribute mass in the near surface, stresses change throughout the critical region and self-similar growth may no longer be possible. Deformation must reorganize in order to "correct" the perturbed topographic shape back to its critical form. This is a well-recognized principle of critical wedge theory [*Dahlen*, 1984; *Willett*, 1992] with consequences at the orogen scale where erosional processes are clearly important.

The processes of erosional feedback described above operate primarily through mass redistribution and consequent changes in gravitational stresses. In addition, crustal deformation can be influenced by the redistribution of heat caused by erosion. As low-temperature upper crustal material is removed by erosion, it is replaced by higher temperature and hence weaker material from depth, potentially leading to localized deformation associated with regions of enhanced erosion.

In this paper I investigate the coupled system of uplift and erosion through the use of a finite element model of deformation and erosion. Finite element models of convergent orogenesis have been based on thin sheet, planform models [*Bird*, 1989;

England and McKenzie, 1982; *England et al.*, 1985], a plane strain assumption [*Willett*, 1992; *Beaumont et al.*, 1992; *Wdowinski and Bock*, 1994; *Fullsack*, 1995], or fully three-dimensional [*Braun and Beaumont*, 1995]. Plane strain models of crustal deformation driven by mantle subduction [*Willett*, 1992; *Fullsack*, 1995] provide the theoretical link to critical wedge theory [*Willett et al.*, 1993; *Willett*, 1999] and have been applied in a variety of settings [*Beaumont and Quinlan*, 1994, *Willett and Beaumont*, 1994, *Beaumont et al.*, 1996a; *Beaumont et al.*, 1996b].

These models have also investigated, to a limited extent, the role of erosion and surface processes. *Beaumont et al.* [1992] developed a two-dimensional (2-D), planform surface process model which they coupled to a finite element model of deformation of the Southern Alps of New Zealand in order to predict the evolution of the topography. The tectonic model used by *Beaumont et al.* [1992] was relatively simple compared to the models of later papers, including this one, but was adequate to demonstrate how topography develops in regions of high uplift and erosion. Other studies have continued to use the Southern Alps as the type example and have used simpler erosion models, but more sophisticated tectonic models in order to investigate the importance of erosion to patterns of exhumation, topography, and cooling rates [Beaumont et al, 1996b; Batt and Braun, 1997]. Other orogenic belts that have been the subject of similar investigations include the European Alps [*Beaumont et al.*, 1996a; *Schlunnegger and Willett*, 1999], the Pyrenees [*Beaumont et al.*, 1999b], the Andes, [*Masek et al.*, 1994] and the Himalayas [*Jamieson et al.*, 1996].

In this paper, I use a plane strain model coupled to a one-dimensional erosion model based on a fluvial, bedrock incision process to systematically document the effects of erosion on orogenic belts to a degree not attempted by the studies cited above. The coupled model is used to demonstrate the dependence of the size, structure, and deformation in the orogen to erosional parameters through the mass balance and critical-topography mechanisms discussed above. The orographic enhancement of precipitation and hence erosion rates is included in the erosion model through the collection of precipitation as river discharge and is important in two aspects. First, the overall increase in erosion rate with an increase in mean elevation tends to bring the system into a stable steady state. Second, orographic perturbation of the regional climate frequently produces an asymmetric pattern of precipitation in systems which have a dominant storm track or wind direction by drawing moisture from storms on one side of a mountain range, leading to the familiar "rain shadow" on the leeward side of mountain ranges [*Barry*, 1981]. I investigate these aspects of orography through two series of models. In the first series, I demonstrate how erosional efficiency affects the overall morphology (size and shape) of a mountain belt and what the resultant patterns of exhumation are. In the second series, I investigate asymmetry in the erosion process and again note the effect on mountain belt morphology and exhumation patterns. Finally, I present two examples of active mountain belts, the Southern Alps of New Zealand and the Olympic Mountains of Washington State to demonstrate how asymmetric precipitation and erosion rate affect the structure of these orogenic belts. These examples were selected because each has been studied extensively and because they provide opposing examples of the effects of the precipitation asymmetry with respect to the polarity of subduction.

2. The Model

The coupled model has a deformation component and a surface-process component. These components are imbedded into a model of orogenesis which assumes that convergent orogens form by crustal detachment and shortening above a subducting substrate consisting of the lithospheric mantle and, in some cases, parts of the lower crust [Willett et al., 1993]. This mechanical model can explain the large-scale structure of mountain belts which are formed primarily by structural thickening as occurs in subduction forearcs [Silver and Reed, 1988; Brandon et al., 1998], small convergent orogens such as the European Alps [Schmid et al., 1996; Beaumont et al., 1996a] the Pyrenees [Morris et al., 1999; Beaumont et al., 1999b] or the Southern Alps of New Zealand [Beaumont et al., 1996b]. In its simplest form, this process can be represented by deformation of a single layer with boundary conditions as shown in Figure 2. The subducting plate moves with velocity V_p towards the overriding plate, which is held fixed in this reference frame. At point S, the substrate of the moving plate detaches and is subducted. The overriding crustal layer is thereby forced to shorten and thicken, resulting in surface uplift by isostatic compensation of the thickened crust. This assumption regarding the kinematics of the lithospheric mantle isolates the crust as a mechanical system dependent only on the motion of the underlying mantle (Figure 2). The full boundary conditions thus consist of an imposed velocity of V_p for $x<0$ and zero for $x>0$ with the origin taken to be at S. The upper surface of the layer is free of shear stress but may have a mass flux across it in response to erosion. The left and right boundaries are taken to be far removed from the domain of interest. The upper and lower boundaries move in response to crustal thickening and isostatic compensation. The upper surface is free to move in response to crustal thickening or mass removal and addition by surface erosion and deposition. The lower surface moves in response to changes in crustal thickness through a flexural model of isostatic compensation. The flexural isostatic compensation mechanism is implemented by calculating the increased load due to crustal thickening and analytically calculating the resulting deflection of a continuous elastic plate under plane-strain conditions [Turcotte and Schubert, 1982]. A flexural rigidity of 10^{22} N m was used in all models. The deformation and erosion models are described in more detail below.

2.1 Deformation Model

Models of the mechanical and thermal evolution of convergent orogens have increasingly relied on numerical methods such as finite element methods because o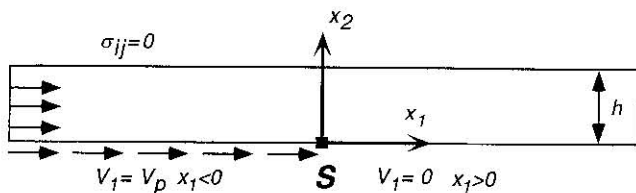f the flexibility afforded by the techniques. Complex domain geometry and constitutive laws describing rock deformation are easily incorporated into finite element algorithms. In addition, the large strains inherent to convergent orogenesis are efficiently modeled by techniques such as the arbitrary Lagrangian-Eulerian technique described in detail by Fullsack [1995]. With this technique, the instantaneous deformation of viscous or plastic materials is modeled in an Eulerian (spatial) frame of reference, while the time-integrated deformation is calculated on a Lagrangian (material) grid which is passively tracked through the time-dependent velocity field. Two of the main advantages of this technique are (1) the virtually unlimited degree of deformation attainable with no degeneration of the numerical solution, and (2) an efficient means for dealing with material fluxes in or out of the model domain.

With the Eulerian formulation, determination of the velocity and deformation requires solution of the Navier-Stokes equation and a conservation of mass equation. The nondimensional form of the Navier-stokes equation, simplified for quasi-steady, momentum free flow is

$$-\frac{\partial \overline{\sigma}}{\partial x_j} + \frac{1}{Ar}\frac{\partial}{\partial x_i}\left(\frac{\partial V_i}{\partial x_j} + \frac{\partial V_j}{\partial x_i}\right) + \delta_{j2} = 0, \quad j=1,2 \tag{1}$$

where $\overline{\sigma}$ is the pressure, V_i are the two components of velocity and Ar is the Argand Number. Summation is implied over repeated indices, and δ_{j2} is defined to be zero for $j=1$ and 1 for $j=2$, representing gravity in the x_2 direction. The definition of Ar depends on the constitutive behavior of the material. For a linear viscous material, Ar is defined as

$$Ar = \frac{\rho g h^2}{\mu V_p}, \tag{2}$$

where ρ is the density, g is the acceleration of gravity, and μ is the viscosity. V_p and h are a characteristic velocity and length, respectively, obtained from the domain and boundary characteristics (Figure 2). For plastic materials obeying a Coulomb yield criterion, Levy-Mises plasticity theory leads to a strain-rate dependent definition of the viscosity, but by assuming that the characteristic strain rate of the system scales with h/V_p, we obtain a Coulomb plastic definition of Ar [Willett, 1999]:

$$Ar = \frac{2}{\tan \varphi}, \tag{3}$$

where φ is the angle of friction of the material. Equation (3) does not completely define the deformation problem, but it demonstrates that the scaling behavior of the plasticity problem depends only on the yield stress of the material, not on the velocity or length scale. To solve the full deformation problem with plastic materials, it is necessary to use the Levy-Mises definition of the plastic viscosity [Willett, 1992; Fullsack, 1995].

For the models in this paper, both plastic and viscous deformational mechanisms are included. Viscous deformation is temperature dependent through an activation energy [Kohlstedt et al., 1995]. Temperature is assumed to be one-dimensional and steady state. Heat production is assumed to vary exponentially with a depth constant of 10 km. A geotherm can be calculated analytically for these assumptions and is time invariant. This model is simplistic but adequate for the purposes of this study, since rheological parameters are not of primary interest. The temperature-dependent viscosity implies

Figure 2. Boundary conditions for the mechanical model. Substrate subduction is inferred to be down to the right, imposing a constant tangential velocity V_p at the base of a crustal layer of thickness h, left of the origin at S. Tangential velocity is zero to the right. Stress on the upper surface is zero.

a variable Ar for the crust, although a depth-averaged value can be used to characterize the strength of the crust [Ellis et al., 1995]. A Coulomb yield criterion is used for the uppermost crust. Plastic and viscous deformation is taken in series so that both mechanisms contribute to strain at any material point, although one mechanism typically dominates. The two forms of the Argand number ((2) and (3)) are thus both applicable at any point in the domain and the effective Ar becomes the sum of the plastic and viscous Argand numbers.   The domain and boundary conditions (Figure 2) define the appropriate scaling parameters in Ar. The characteristic velocity for the problem is the convergence velocity, V_p and the characteristic length is the layer thickness h. These are the appropriate values in the Argand number and are used to nondimensionalize space $(x^*=x/h)$ and time $(t^*=tV_p/h)$ in (1). The scaling of the deformation problem has been investigated elsewhere [Ellis et al., 1995; Willett, 1999], but these scaling relationships will be used for analysis of the erosion model of the next section.

The boundary value problem defined by these conditions and material properties is solved by a finite element method as described by Fullsack [1995].

With no erosion, the boundary conditions of Figure 2 produce convergence, crustal thickening and hence topography as shown in Figure 3. Figure 3 shows a model result in a format that will be followed throughout the paper. Instantaneous and net deformation are shown at three stages of evolution as denoted by the nondimensional time, t^*. Nondimensional time units correspond to total convergence in units of the layer thickness, so that a nondimensional time of two $(t^*=2)$ corresponds to convergence of twice the layer thickness. Instantaneous deformation is shown by the shaded levels of nondimensional strain rate; the second invariant of the rate of deformation is the scalar quantity shown. Net deformation is given by the Lagrangian mesh. Deformation in the model of Figure 3 is initially localized at the plate boundary (point S in Figure 2). With increasing convergence,
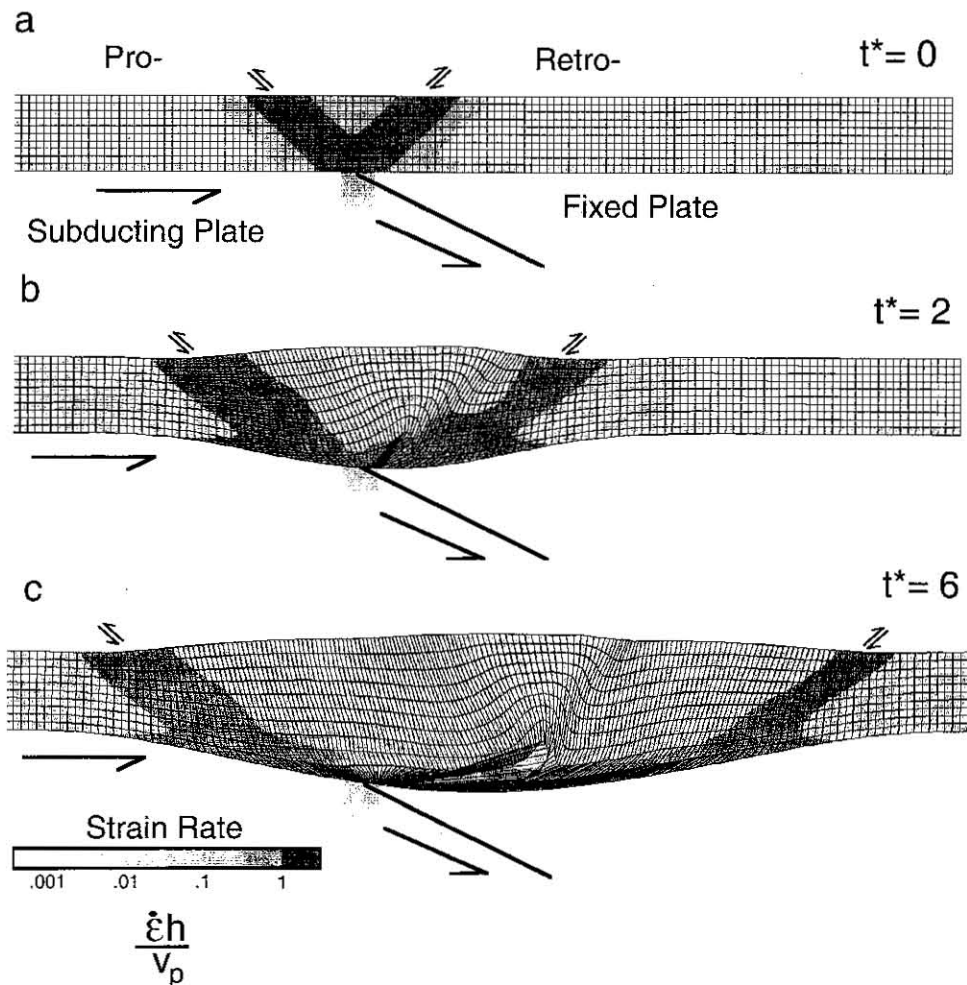

Figure 3. Finite element model for viscous-plastic deformation during convergence with no erosion and the boundary conditions shown in Figure 2. Model results are shown at nondimensional times t^* of 0, 2 and 6. The following features apply to this and all subsequent models. Substrate detachment point is given by the grey rectangular block. Crust deforms according to a temperature-dependent viscous constitutive law below the Coulomb yield stress. Viscous strength is characterized by an Argand number of 0.5 at the base of crustal layer prior to deformation. A Coulomb friction angle of 15° is used. Instantaneous deformation is given by shaded levels of the second invariant of nondimensional strain rate. Total deformation is shown by the Lagrangian tracking mesh. Note that no calculations are made on the Lagrangian mesh. The upper surface of the model is indicated by the top of the shaded region and the bold line. Surface does not coincide with the top of the Lagrangian mesh in the presence of erosion or sedimentation.

the region of deformation propagates outward with the formation of back-to-back orogenic wedges characteristic of this type of model (Figures 3b and 3c). The taper angles and surface slope angles of these wedges depend on the rheological parameters as described above. For dominantly Coulomb plastic crustal rheology, the orogenic wedges attain the theoretical critical wedge geometry [*Davis et al.*,1983; *Dahlen*, 1984]. However, in the early stages of development, the wedge above the downgoing plate (prowedge) (Figure 3, left) attains the minimum taper angle, whereas the wedge above the overriding plate (retrowedge) is steeper with a taper angle at the maximum critical taper [*Willett et al.*, 1993; *Wang and Davis*, 1996] (Figure 3b). This different mechanical behavior on either side of the detachment point motivates the use of the pro- and retro- prefixes that are used in this paper to refer to features of the respective wedges. With increasing convergence, crustal thickening leads to warming of the lower crust and reduction of the lower crustal viscosity. The lower viscosity produces two effects. First, it decreases the asymmetry in the topography, resulting in similar slopes on the flanks of the orogen, and second, it results in a maximum elevation of the orogen and the formation of a high-elevation plateau in the orogen interior [*Willett and Beaumont*, 1994]. This latter effect is a direct consequence of lateral flow in the lower crust preventing any additional increase in crustal thickness and elevation [*Bird*, 1991; *Royden*, 1996]. The degree of convergence at which the orogen begins forming a plateau depends on the Argand number of the system. Although the temperature dependence of the viscosity precludes the specification of a constant Ar, using the minimum viscosity in the initial configuration of the crust in the model of Figure 3 gives Ar less than 0.5, implying a strong crust [*Willett*, 1999].

The mixed plastic and viscous rheology precludes the calculation of an analytical solution to the stresses and geometry of the model orogenic wedges, but the principle of critical topography is still applicable. The topography developed in the model is "critical" in the sense that the topographic slopes are the minimum required to allow deformation to persist throughout the wedge and propagate outward with continued convergence. The viscous deformational mechanism introduces velocity dependence into this topography through the Argand number. The internal and topographic structure of the orogen at all scales of growth depends on the polarity of subduction. Deformation of the crust results from continued accretion of material from the underthrusting plate onto the overriding plate, i.e., through the prowedge into the retrowedge. This mass flux by accretion results in net motion, or advection, of structure to the right into the retrowedge and produces the asymmetric internal structure apparent in Figure 3. This horizontal velocity field also produces topographic advection contributing to the topographic asymmetry, a mechanism discussed in more detail with the coupled models.

2.2 Erosion Model

Although many erosional processes are important in evolving landscapes, in high relief, high uplift areas such as active mountain belts, the number of important processes is limited. In the Southern Alps of New Zealand, *Hovius* [1995] and *Hovius et al.* [1997] found that two processes could account for all mass eroded and removed from the system:

fluvial incision and bedrock landslides. Fluvial incision dissects actively uplifting regions and creates local relief in the form of deep mountain valleys. Mass wasting in the form of bedrock landslides moves material from hillslopes onto the valley floors, where rivers can transport it out of the system. *Densmore et al.* [1998] came to a similar conclusion based on numerical modeling of Basin and Range topography; realistic model topography was only obtained for a model that included landsliding and fluvial incision as the dominant mechanisms.

Bedrock landslides and other hillslope processes are responsible for the size and shape of interfluves separating river valleys. However, it is the rivers that control the regional rate of erosion through the process of bedrock incision. As rivers incise valleys, local relief increases, thereby accelerating the rate of hillslope erosion. River and hillslope erosion rates quickly achieve a balance, particularly at high uplift rates so that characterizing the rate of fluvial incision is equivalent to characterizing the downcutting rate of the entire landscape. For this reason, I limit consideration of erosion to the fluvial incision process. This assumption restricts the predictive capability of the models in that they cannot address geomorphic characteristics of the landscape such as the shape and size of interfluves, the development and topology of drainage networks, or the specific shape of longitudinal river profiles, but does not limit the prediction of orogen-scale erosion rates and distributions.

The process of fluvial incision into uplifting bedrock is not well understood, but geomorphologists have long proposed that incision will depend primarily on channel slope, river discharge and rock type [e.g.,*Gilbert*, 1877]. *Howard and Kerby* [1983] cast this into a quantitative erosion law in an empirical form with the erosion rate $\dot{e}$ defined as

$$\dot{e} = k_a A^m \left| \frac{dh}{dx} \right|^n , \tag{4}$$

where A is the drainage basin area taken as a proxy for river discharge, $\left| \frac{dh}{dx} \right|$ is the magnitude of the local river slope, and k_a, n, and m are empirical parameters. The exponents n and m take specific values for theoretical cases such as erosion rate proportional to bed shear stress ($m=1/3$, $n=2/3$) [*Howard and Kerby*, 1983] or stream power ($m=n=1$ with river discharge, Q proportional to A), but more commonly, parameters are determined by empirically fitting models to river longitudinal profiles. The exponent on area, m, also attains different values depending on whether erosion rate varies with mean annual discharge (m is close to 1) or peak discharge during flood events (m is typically less than 1) [*Leopold et al*, 1964]. It might also reflect a downstream increase in channel width, reflecting the reasonable assumption that erosion rates increase with discharge per unit width rather than total discharge. Unfortunately, there are virtually no data on the systematic variations of width of bedrock channels, particularly in actively uplifting regions. The proportionality constant k_a reflects the physical erodibility of the channel bed and the average precipitation rate in the drainage basin, although the specific interpretation of k_a, as well as its dimension, varies depending on the specific physical processes represented by (4).

The physical parameters in (4) have been estimated by several methods in a variety of settings. Howard and Kerby [1983] analyzed badland channels and found a best fit $m=0.45$ and $n=0.7$. *Seidl and Dietrich* [1992] presented data from the Oregon coast ranges that support an n/m ratio of 1. In a later

study of river profiles in Kauai, *Seidl et al.* [1994] concluded that erosion rates were proportional to stream power ($n=1$, $m=1$). More recently, *Stock and Montgomery* [1999] reviewed a number of studies and reanalyzed data from a number of sites to estimate erosion parameters. They concluded that most rivers supported an area exponent, m of 0.3 to 0.5 and a slope exponent, n, of 1.0. In addition, using these exponents, they found that k_a varied from 10^{-7} to 10^{-2} $m^{0.2}$/yr, depending on rock type.

A remaining question involves the dependence of incision processes on sediment load in a river. With high suspended sediment concentrations and bed load, it is expected that, all else being equal, river incision rates should decrease due to the increased bed coverage by temporarily stationary sediment. This has been included in some formulations by modeling fluvial incision rate proportional to excess-stream power [*Chase*, 1992; *Beaumont et al.*, 1992; *Densmore et al.*, 1998; *Braun and Sambridge*, 1997], defined as the difference between river capacity which is dependent on stream-power and local sediment flux, qs:

$$\dot{e} = k_I\left(k_r Q \left| \frac{dh}{dx} \right| - q_s \right)$$ (5)

The first term inside the parentheses is the carrying capacity of the river, so that as the sediment flux approaches capacity, the incision rate goes to zero. There is a second theoretical dependence of incision rate on sediment load due to the abrasion of the bed by sediment. Theoretically this process implies an increase in incision rate with increased sediment load (opposite in sign to the effect described in (5)) [*Sklar et al.*, 1996; *Slingerland et al.*, 1997]. There are few or no data on this process, although it is likely to be most important at relatively low values of sediment flux.

Lacking a well-accepted and well-calibrated model for fluvial incision is problematic for modeling studies which depend on a quantitative erosion model. In the absence of a definitive model, most modeling studies have simply included a linear dependence on stream power ($n=1$, $m=1$)[*Chase*, 1992; *Beaumont et al.*, 1992; *Anderson*, 1994; *Kooi and Beaumont*, 1994; 1996; *Tucker and Slingerland*, 1994; *Densmore et al.*, 1998]. Although simplistic, the linear model captures the important physical processes and parameter dependencies. Most important for this study, it provides the feedback mechanisms between orogen growth and erosion. Tectonic uplift of the surface increases slope; outward growth of elevated topography increases drainage area and hence discharge. Either case leads to an increase in erosion rates.

Other values of m or n lead to differences in river profiles, but all reasonable values predict concave-up profiles so that for a river basin of given scale, these parameters are of second-order importance.

The behavior of the stream-power erosion law can be illustrated by the analytical solution to the simple problem of a finite width block with constant surface uplift rate (Figure 4). If the discharge increases linearly downstream, as occurs with a rectangular drainage basin and a constant precipitation rate, the linear form of (4) is,

$$\dot{e} = k x_r \left| \frac{dh}{dx} \right|,$$ (6)

where x_r is the distance from the water divide and k, the proportionality constant, is a function of precipitation rate and has a dimension of 1/time.

Given a block of width $2L$ uplifting at a constant rate of u, the elevation is described by solution of the nondimensional equation:

$$\frac{dh^*}{dt^*} = N_e x^* \frac{dh^*}{dx^*} + 1,$$ (7)

where h^* and x^* are nondimensional height and distance, each normalized by L; t^* is nondimensional time, defined as $t^* = ut/L$, and N_e is a characteristic number, $N_e = kL/u$, which I will refer to as the erosion number. The erosion number N_e is a ratio of the rates of erosion and tectonic uplift, thereby characterizing the effectiveness of the fluvial incision process relative to the uplift. With boundary conditions of $h^*=0$ at $x^*=\pm 1$, the solution of (6) is

$$h^*(x^*,t^*) = \begin{cases} t^* & x^* < exp\left(-N_e t^*\right) \\ \dfrac{-\ln\left(x^*\right)}{N_e} & x^* \geq exp\left(-N_e t^*\right) \end{cases}.$$ (8)

At steady state this reduces to simply

$$h^* = -\frac{1}{N_e} \ln(x^*),$$ (9)

as shown in Figure 4. The logarithmic function for the longitudinal profile of transverse rivers is typical, although not universal, in active mountain belts [*Hovius*, 1995].
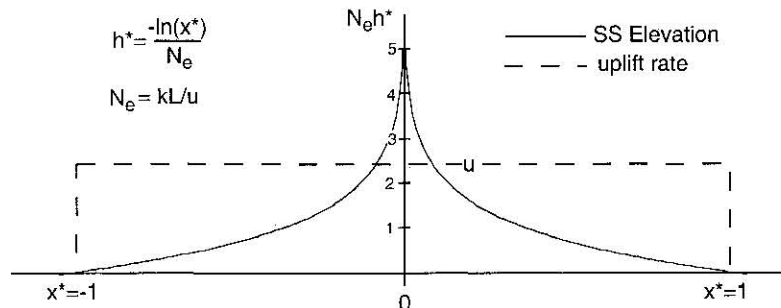

Figure 4. Fluvial incision model demonstrated for case of constant uplift rate of u over a domain of width $2L$. Erosion rate is proportional to stream power with a linear downstream increase in discharge. Steady state solution is a logarithmic function of x^* scaled by the erosion number N_e.

3. Coupled Model Results

Combining the erosion model and the mechanical model is straightforward. The 1-D erosion model (6) is applied to the upper surface of the 2-D finite element model, which provides vertical and horizontal components of velocity. In all models, it is assumed that there is a series of transverse rivers on each side on the topographic divide. These rivers flow from the point of maximum elevation to the edge of the model. In the event that there is a closed basin, as occurs in the flexural moat surrounding the uplift, these basins are filled to the elevation of the basin lip. This permits the rivers to cross the basins and transport sediment out of the system. No attempt is made to conserve or calculate the eroded mass; it is assumed that the volume of the eroded sediment is large enough to fill the surrounding foreland basins, with much of the material bypassing these to an unspecified deposition site.

3.1 Erosional Efficiency

As the simple analytic solution of (9) demonstrates, the equilibrium size and shape of a mountain belt reflect the balance between uplift rate and the efficiency of the erosion (fluvial incision) process. This is reflected in the definition of the erosion number N_e, the characteristic number for the uplift-erosion problem defined in (7). For the 2-D coupled problem, N_e takes a slightly different form. Nondimensionalizing the erosional problem using the layer thickness h as the characteristic length scale and h/V_p as the characteristic time as was done for the deformation problem yields

$$N_e = \frac{kh}{V_p}, \tag{10}$$

with V_p and h defined in Figure 2 and k reflecting the bedrock incision efficiency and the precipitation rate. However, there is an alternative analysis, as there is a second length scale introduced into the problem through the erosion law which depends on the length of a drainage basin which is approximately half the width of the orogen. Defining the orogen width as $2L$ as in the analytic solution above, there are two characteristic fluxes in the system: the accretion mass flux reflecting convergence,

$$F_a = V_p h,$$

and the erosional flux out the upper surface, which from (6), scales as

$$F_e = 4kL^2.$$

The erosion number N_e can be interpreted as reflecting the ratio of these fluxes:

$$N_e^* = \frac{4kL^2}{V_p h}. \tag{11}$$

N_e^* differs from N_e by the inclusion of a horizontal length scale. However, this horizontal length scale is problematic in that, in general, it is not constant with time. Orogen width is a function of time so that although initially L will be of the order of h, it will increase with convergence and the accretion of new material into the orogen. The length scale L is only constant if the system is in steady state. The time dependence can be

isolated in a nondimensional parameter by using the ratio of the crustal thickness and the horizontal length scale:

$$\gamma = \frac{h}{2L},$$

giving,

$$N_e^* = \frac{1}{\gamma^2} N_e. \tag{12}$$

The two forms of the erosion number given by (10) and (11) represent the same scaling behavior of the system but are used slightly differently. Equation (10) has an explicit definition in terms of time-independent tectonic parameters and so provides a useful characterization of a model or other system where time dependence is treated explicitly. This form of N_e will be used to characterize all models in this paper. The second form of N_e (11) is more appropriate if the orogen width is large compared with the crustal thickness and where N_e is to be used to characterize erosional fluxes. With either definition, N_e reflects the scaling behavior of the coupled problem in that a small N_e reflects a convergence and uplift dominated system in which erosion rates are low either due to incision-resistant rock or low precipitation rate. A large N_e reflects an aggressive erosional environment in which uplift is unlikely to produce high elevation topography. The model with no erosion (Figure 3) represents the case of $N_e= 0$. In the limit as $N_e \to \infty$, no topography can exist; erosion is efficient to the point of destroying any increase in elevation above base level.

In practice, N_e lies in a small range of values; convergent tectonics creates topography with elevations over a kilometer but under 10 km, suggesting that under typical conditions, the tectonic accretionary flux does not greatly exceed the erosional flux. This small range is the result of the local feedback between uplift and climate. Larger topography results in higher orographic precipitation rates and hence increased erosion rates reflected in a higher value for N_e. In addition, an increase in topography also results in an increase in orogen width and hence catchment size. A larger catchment increases river discharge and thereby enhances erosion rates in downstream reaches. There is also a mechanical limit to topography, but this seems to be reached only for very large orogenic belts such as the India-Asia collision, which has resulted in the formation of the Tibetan Plateau. Relief of smaller orogenic systems appears to be limited by erosion or the duration and magnitude of shortening.

A coupled model with $N_e=2$ is shown in Figure 5. Mechanical parameters are the same as in Figure 3; the only change between the models of Figure 3 and Figure 5 is the addition of surface erosion. Erosion is applied according to (6) with k constant across the entire model, implying a constant precipitation rate as well as uniformly erodable material. The amount of material eroded is given by the projection of the Lagrangian mesh above the ground surface; this surface is given by the bold line at the top of the Eulerian mesh. The actual position of the nodes of the Lagrangian mesh above the model surface is not significant, since there is no meaningful way to calculate material point motion above the surface, but the intersection of the Lagrangian mesh and the upper surface of the Eulerian mesh provides a measure of the exhumation that would be observed at the surface. Exhumation is defined in these models as the original, predeformation depth of material currently at the surface and is calculated by
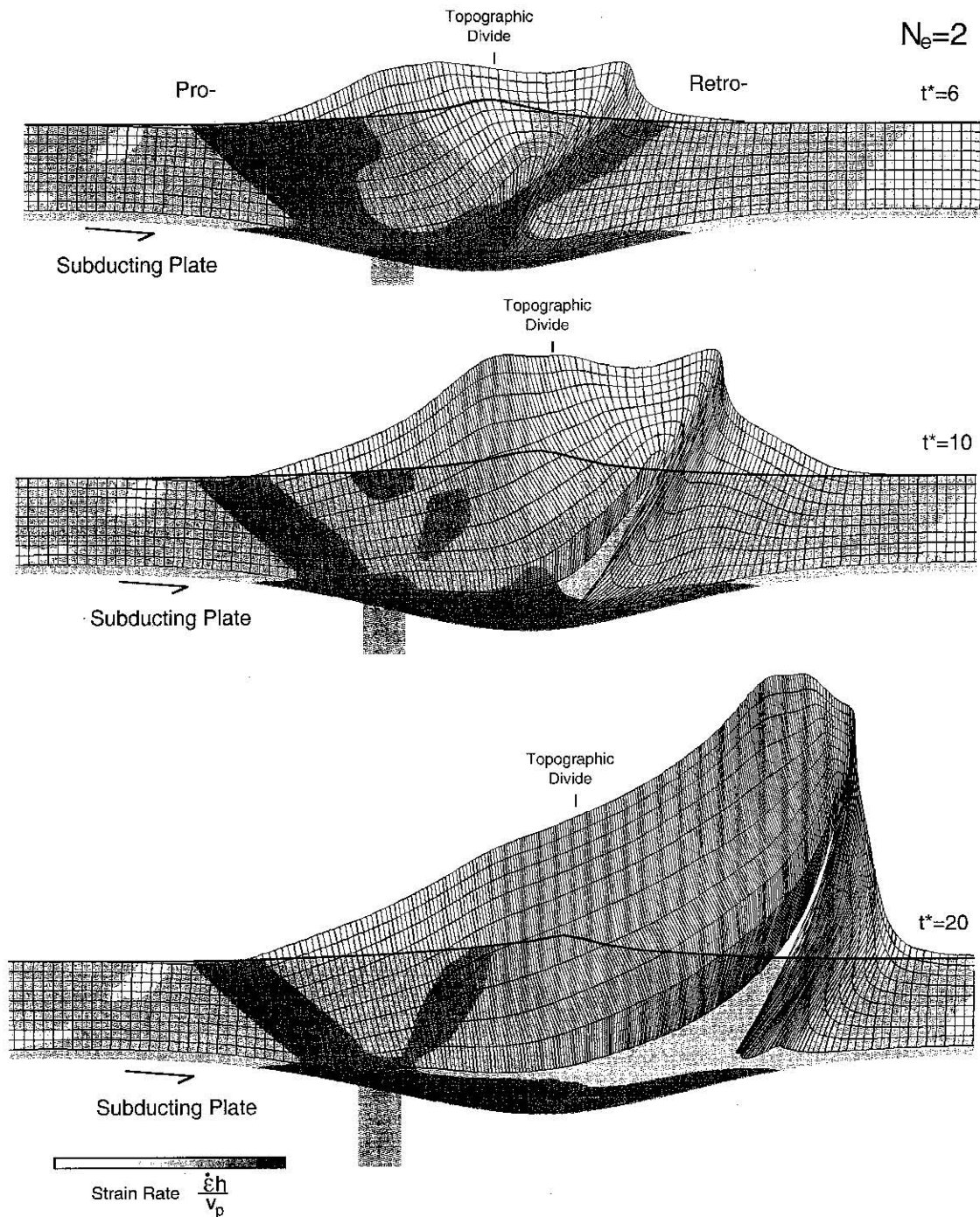
Figure 5. Coupled deformation and erosion model characterized by an erosion number N_e of 2.0. Precipitation rate is constant across the model. Total exhumation is indicated by the extension of the Lagrangian mesh above the model surface which is given as the top of the grey-shaded domain. Bottom row of Lagrangian elements has been omitted for clarity. Results are shown at nondimensional times t^* of 6, 10, and 20. See Figure 3 caption for additional model description.

interpolating the upper (Eulerian) surface onto the Lagrangian grid and determining the original depth of the material point. It is not therefore a measure of the maximum depth of burial as it does not account for any increase in burial that occurs as material is transported through the deforming orogen. This calculation of exhumation is sometimes problematic, as deformation of the Lagrangian mesh can be extreme, particularly in the vicinity of the retrodeformation front, where individual elements might actually fold over themselves or other elements.

This presents no numerical problems, as the Lagrangian mesh is not used for any calculations, but it can make reconstruction of the depth of burial difficult, and specific estimates of exhumation in these regions of high strain should be treated with some caution.

Figure 5 shows the evolution of the model through three stages at nondimensional times of 6, 10, and 20. The surface elevation reaches a steady state after a nondimensional time of about 12. It is important to note that steady state implies no

change in elevation with respect to the datum with time. This is an Eulerian definition in that any specific material point can still be moving in either dimension, either tangential to the surface in the absence of local erosion or toward the surface in the presence of erosion. In two or higher dimensions, steady state is not defined by the condition of surface uplift and erosion rates being equal because of the possibility of horizontal mass transport balancing erosion or vertical rock uplift. Rock uplift or exhumation is an independent function and therefore reaches a steady state at a time independent of the surface elevation. In this case, exhumation is not in steady state until the lowermost crust is exposed at the surface, which occurs at a time of about 20 (Figure 5, bottom). The development toward steady state can be seen more clearly in Figure 6, which shows the evolution of the surface elevation and exhumation. Each of these evolves toward a steady state which is attained sooner by the surface elevation.

The elevation in this model exhibits the concave-up, logarithmic shape characteristic of the analytical solution to a constant uplift, stream-power erosion law (Figure 4). However, the profile is not symmetric. The retrowedge retains the steeper slope that was also characteristic of the noneroding case (Figure 3). Note also that the entire orogen is offset to the

right from the detachment point S. This is the result of the overall left-to-right sense of motion within the system.

The pattern of exhumation also reflects this left-to-right (pro-to-retro) motion of material. This pattern is highly asymmetric, with a gradual left-to-right increase in the original depth exposed at the surface and a much sharper rate of increase from the right edge of the orogen to the deepest exposed material. Material from the greatest depth, representative of the highest grade metamorphic rock in an orogen, is exposed at low elevation at the retrodeformation front. This pattern of exhumation reflects the sense of subduction and mass accretion and is a fundamental characteristic of this type of model.

An increase in the efficiency of erosion predictably leads to a system that reaches steady state much more quickly (Figure 7). With an erosion number N_e of 10, the elevation reaches a steady state after a nondimensional time of under 2. Exhumation again takes longer to reach steady state but has equilibrated after a time of about 6. The increase in erosional efficiency also decreases the total elevation, from a maximum elevation of $0.25h$ with $N_e = 2$ to a peak elevation of $0.15h$ with $N_e = 10$. The cross-sectional shape is again sharp, with concave-up slopes and is slightly asymmetric with a steeper retrowedge.

It is not surprising that the surface of this model develops a structure similar to the analytic solution of Figure 4 given the small size of the orogen in Figure 7. With little outward growth of the orogen, there is little internal deformation of the triangular block between the limiting shear zones, which is thus passively uplifted and transported to the right at a near-constant rate. In fact, it is close enough to a constant uplift rate to compare the elevation directly to the analytic solution of (7) although N_e must be adjusted by the ratio of orogen width to thickness, γ, as described in (12). In this model, $\gamma = 1.6$. The numerical and analytical solutions (Figure 8) differ primarily in the asymmetry introduced by the horizontal motion but agree in overall magnitude of elevation and general shape.

A decrease in N_e to 1.0 represents a relative decrease in erosional efficiency, leading to a much larger orogen which requires much longer to achieve steady state (Figure 9). Even after total convergence of $30h$ (Figure 9) exhumation patterns are still changing, albeit slowly. This model was run to a dimensionless time of 60 and was still showing small changes in exhumation, although the elevation appeared to be steady. The steady state elevation indicates that the low erosion rate results in a broadening of the orogen and an increase in the drainage basin size, particularly on the prowedge, as the topographic divide migrates far to the right in Figure 9. The increase in drainage basin size increases the discharge and hence total erosional flux until steady state is achieved. It is important to note that the erosional flux might also have increased through an increase in elevation and hence slope. The fact that the steady state balance was achieved largely by basin area increase is likely a result of the mechanical limit to total elevation that was apparent in the model of Figure 3. With stronger material, an orogen might reach higher elevation and thereby achieve steady state by the increase in average slope.

The effects of the mechanical limit to elevation are apparent in a comparison of the steady state elevation profiles (Figure 10). At large N_e, the elevation profiles are dominated by the fluvial erosion process and take the form of the concave-up river profile inherent to this process. However, as N_e decreases to 1.0, this form is lost, and the broad, more plateau-like form characteristic of the mechanical process is attained. In the
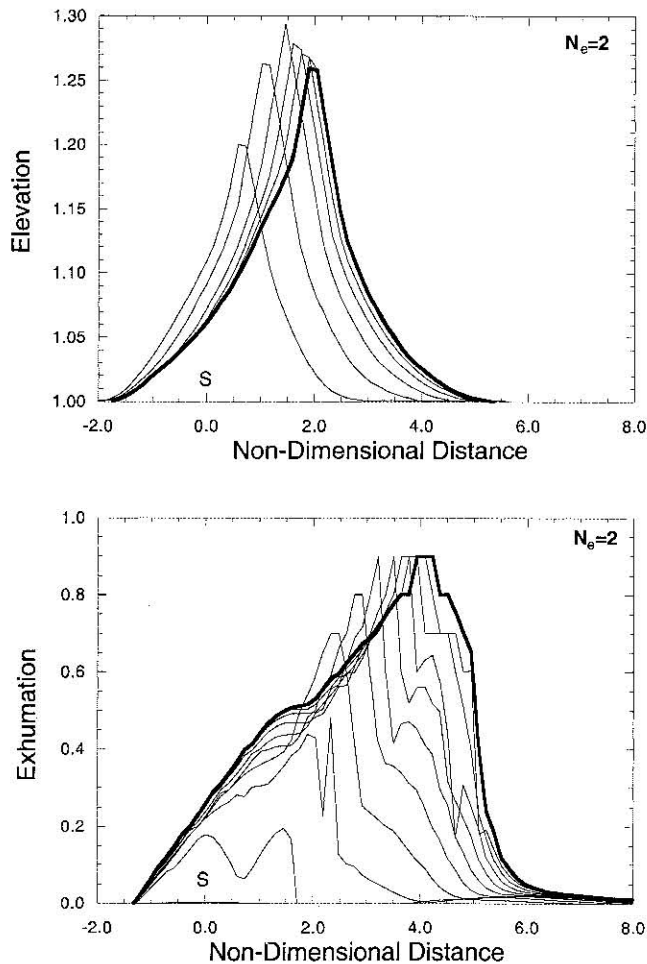

Figure 6. Nondimensional exhumation and elevation as a function of nondimensional time and distance for the model shown in Figure 5. Nondimensional time increment is 2. Bold curves represent final, near steady state conditions. Note that elevation reaches steady state before exhumation.
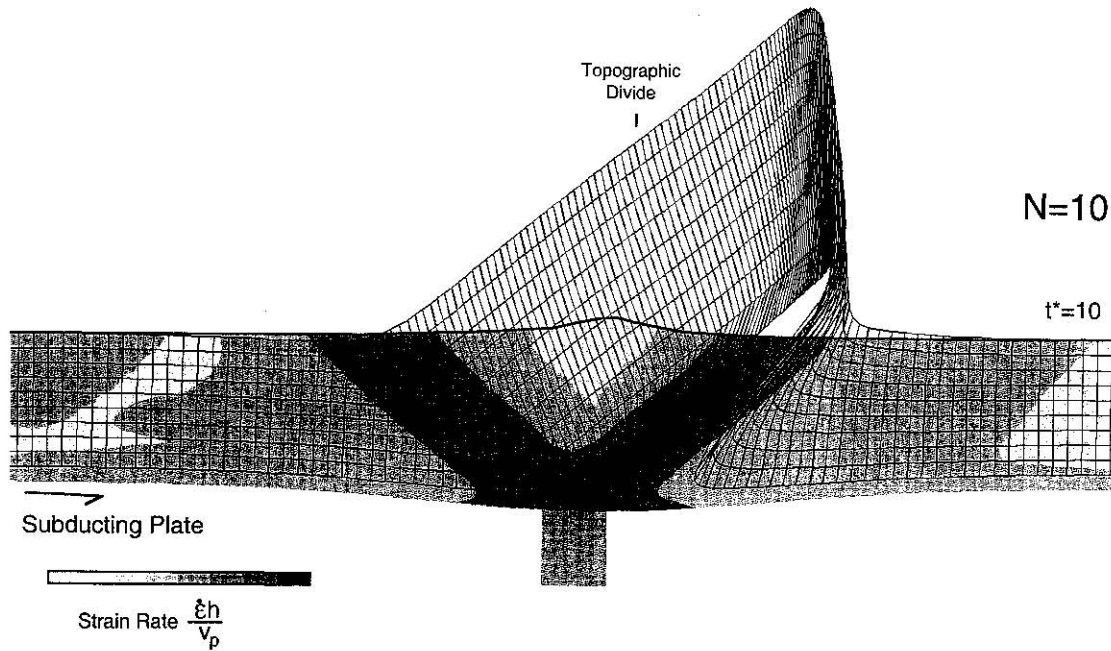
Figure 7. Coupled deformation and erosion model characterized by an erosion number N_e of 10. This is an erosion-dominated system with little excess elevation. Results are shown at nondimensional time t^* of 10. Elevation and exhumation have reached steady state. See Figure 3 caption for additional model description.

complete absence of erosion, no steady state can be achieved, so the model with N_e =0 is shown at 4 times and would continue to grow outward with increasing time without a large increase in maximum elevation.

3.2 Orography and Rain Shadows

The models of the previous section demonstrate the effects of erosional feedback in the sense of enhanced erosion rates in regions of high elevation, but this effect is typically not as uniform as is applied in these models. The models in the previous section include only erosional enhancement due to the increase in drainage basin size and the increase in slope but do not consider the effects of spatially variable

Figure 8. Comparison of steady state elevation of model of Figure 7 and analytical solution of Figure 4. Nondimensional domain length L of 1.6 is used for the analytic solution. Note asymmetry in the numerical solution resulting from the horizontal velocity.

precipitation rates. Orographic precipitation effects commonly include an asymmetric distribution resulting from the disruption of a storm track by high elevation mountains. When storm systems encounter a topographic barrier, moisture-laden air is forced to rise, leading to decompression, saturation, and precipitation [*Barry*, 1981]. Much of the moisture in the air mass is lost during this initial rise so that precipitation on leeward slopes of a mountain range is much reduced. The result is a mountain range with a wet climate on the windward side and a dry climate, commonly referred to as a rainshadow, on the opposing leeward side. The geologic effects of rainshadow systems have been noted in the Southern Alps of New Zealand, where the orographic asymmetry is very pronounced [*Wellman*, 1979; *Koons*, 1989; *Beaumont et al.*, 1992]. In other cases, orographic precipitation may be enhanced in magnitude but without the asymmetry in distribution, as for example, in Taiwan, where uplift has led to very high precipitation and erosion rates but no clearly defined rainshadow.

The interaction of an asymmetric orographic system with the mechanical orogen model described above is particularly interesting because of the polarity inherent to a subduction-driven system. Given the two possibilities for orogen wedge mechanics, retrowedge on the overriding plate or prowedge on the subducting plate, and the two possibilities for orographic climate (wet and dry sides), there are two asymmetric combinations: wet retrowedge or wet prowedge.

The case with precipitation focused on the retrowedge is simulated in the model of Figure 11. This model represents the end-member case of infinitely efficient precipitation extraction so that all precipitation is on the windward slope and there is no precipitation to the left of the topographic divide. On windward slopes the precipitation rate is constant. A characteristic erosion efficiency N_e of 2 is used. Although this is the same value of N_e as used in the model of Figure 5, the orogen in this case is much larger because the erosion is
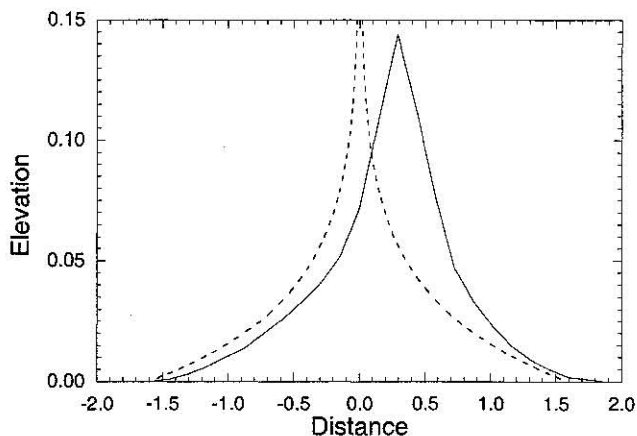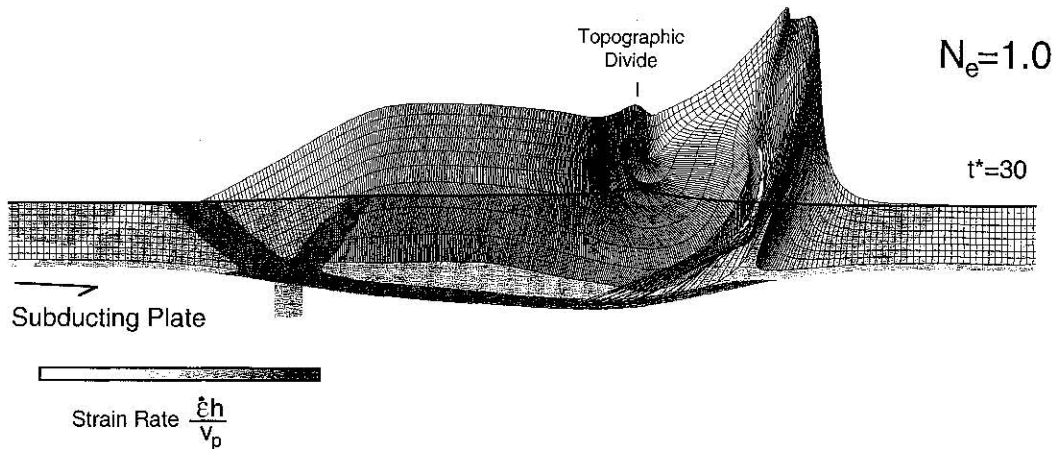
Topographic Divide

$N_e=1.0$

$t^*=30$

Subducting Plate

Strain Rate $\frac{\dot{e}h}{V_p}$

Figure 9. Coupled deformation and erosion model characterized by an erosion number N_e of 1.0. This is an uplift dominated system with low erosion rates. Results are shown at nondimensional time, t^* of 30. Steady state has not yet been achieved. See Figure 3 caption for additional model description.

applied over only half (the windward side) of the system. The morphology shows some influence of the asymmetric erosion (Figure 12), although at these erosion rates, topography does not differ greatly from the symmetric case. Exhumation shows the influence of the erosion distribution more clearly. With exhumation confined to the steep retrowedge and erosion rates high enough to match convergence flux, the entire crustal layer is exhumed over a relatively short distance. Although the exhumation still exhibits the pattern of gradual increase on the prowedge side and rapid increase on the retrodeformation front, the entire pattern is highly compressed relative to the previous models. In particular, the exhumation front at the retrodeformation front is very sharp, with deeply exhumed material closely juxtaposed with undeformed, surface material. Exhumation is zero on the prowedge, left of the divide, and in fact, the small amount of deposition that occurs in the foreland depression in front of the deformation front is carried into the orogen by the horizontal motion; this is seen as the upper section of the prowedge with no Lagrangian mesh.

The contrasting case of the windward, wet climate applied to the prowedge side of the orogen is shown in Figs. 13 and 14. The focusing of precipitation and incision on the prowedge leads to an increase in catchment area on the windward side of the orogen as the topographic divide migrates away from the direction of precipitation. This divide migration is in the same direction as the tectonic motion, so the divide moves rapidly to the right (Figure 14), further increasing catchment area and discharge. This increases erosion rate, particularly near the prodeformation front, where continued accretion keeps the surface slope high. By $t^*=18$ nearly all erosion is occurring near the toe of the prowedge, so that the system is nearly in steady state with the accreted mass nearly balanced by the erosion occurring within a short distance of the deformation front (Figure 13, bottom). With deformation and surface uplift focused at the prodeformation front, the orogen interior and retrowedge become detached from the tectonically driven deformation. The strain rate in the retrowedge has decreased nearly an order of magnitude over the duration of the model. Erosion rates are also quite low at distances greater than about $2h$ right of point S, but left of the divide. However, this model never quite reaches steady state, even after a time of 32. The topography develops a high plateau with a very low slope and

low erosion rates. Deformation rates in this plateau and the retrowedge to the right are very low but never zero. This is likely the result of the artificial boundary conditions that allow no erosion to the right of the divide, thereby allowing it to continue migrating to the right, increasing the catchment area. Note also the decrease in maximum elevation as the catchment size increases and lower slopes are required to achieve the same erosion rate. Presumably a steady state would be achieved eventually, but this would require that the excess elevation near the divide be removed by mechanical or erosional processes, leaving a broad, low slope catchment across the prowedge and most deformation focused at the deformation front. At steady state, the retrowedge would be completely nondeforming, as it would be isolated from the flux of material in the accretion-erosion system which is confined to the prowedge.

The most important difference between the models in Figures 13 and 11 is the pattern of exhumation relative to the orogen
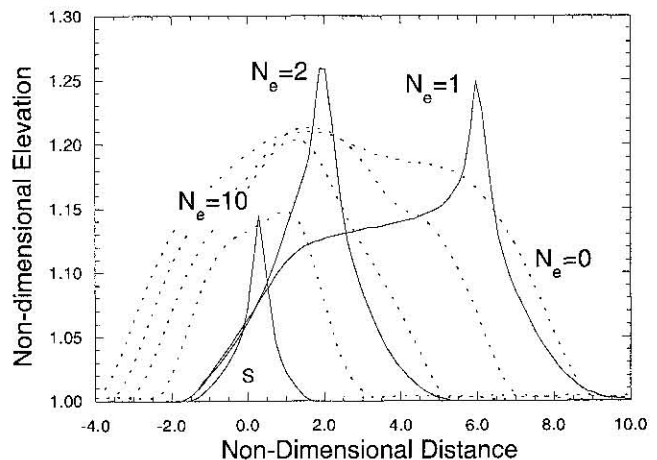

Figure 10. Comparison of steady state elevation profiles as a function of erosion number N_e. Corresponding models are shown in Figures 5, 7, and 9. Dashed lines show elevation profiles in the absence of erosion for model in Figure 3 at nondimensional time increments of 2.0.
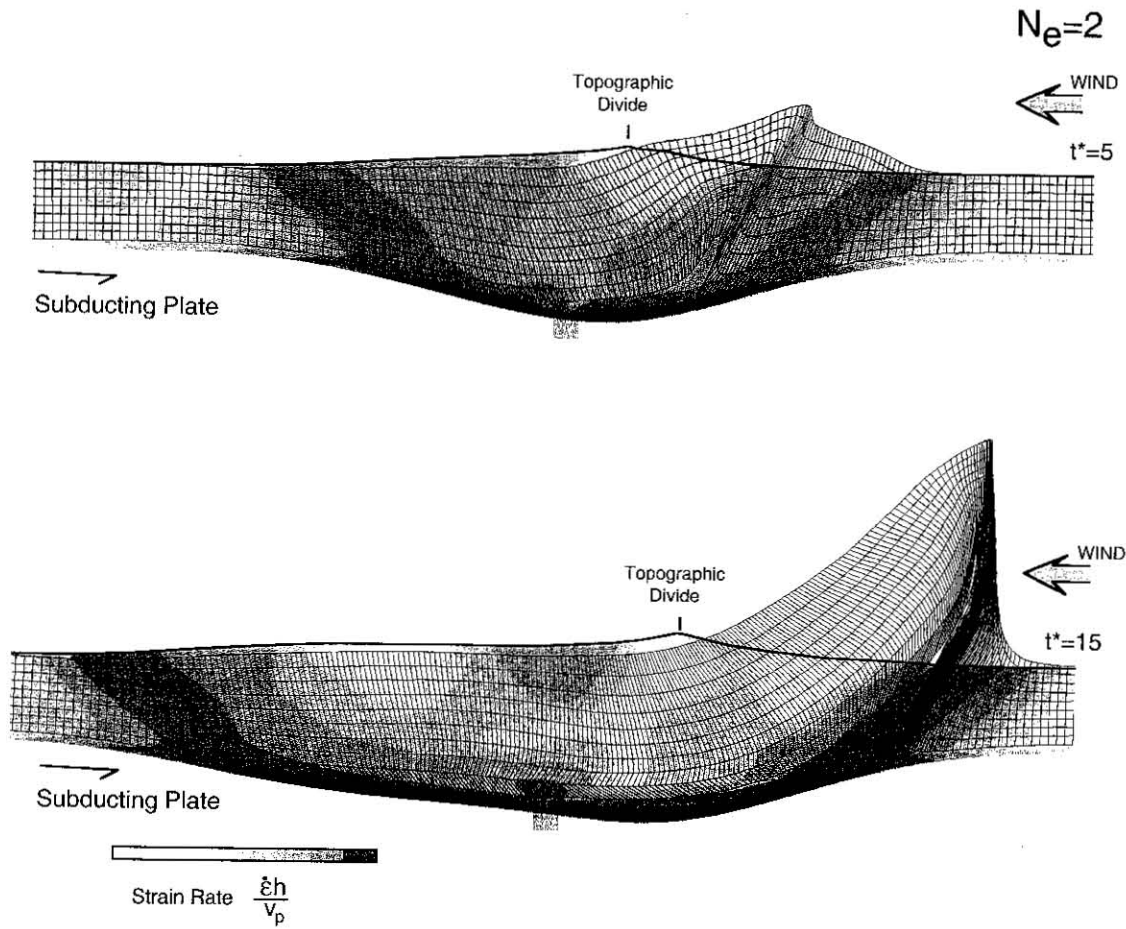
$N_e = 2$

WIND

$t^* = 5$

Topographic
Divide

Subducting Plate

WIND

$t^* = 15$

Topographic
Divide

Subducting Plate

Strain Rate $\dfrac{\dot{\varepsilon}h}{v_p}$

Figure 11. Model with precipitation focused on retrowedge. Retrowedge is characterized by an erosion number N_e of 2.0. Prowedge has no erosion ($N_e = 0$). Results are shown at nondimensional times t^* of 5 and 15. Steady state has been achieved by t^* of 15. Bottom row of elements has been omitted for clarity. See Figure 3 caption for additional model description.

structure and topography. In the case of prowedge erosion (Figures 13 and 14) erosion results in a broad domal exhumation pattern distributed across the prowedge interior. There is no clear exhumation front, at least in the model of Figure 13, but exposure of the deepest rocks is clearly in the interior of the orogen. This is in contrast to the model of Figure 11, which exhibits a clear, strong exhumation front at low elevation at the retrodeformation front. Even in the absence of any topography, for example, in an ancient, fullyeroded orogenic belt, this difference should be evident in
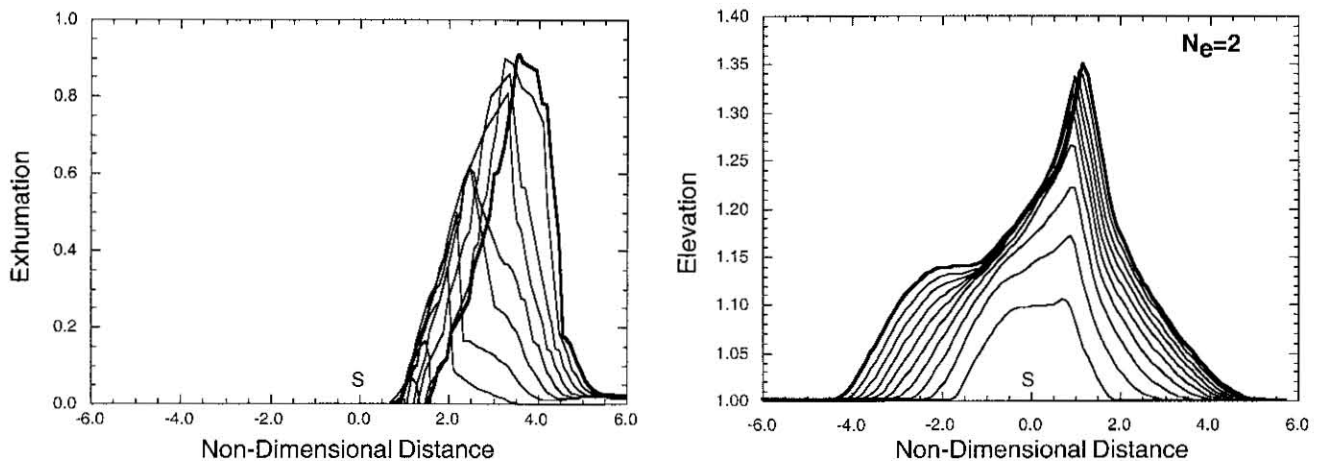
Figure 12. Nondimensional exhumation and elevation as a function of nondimensional time and distance for the model shown in Figure 11. Nondimensional time increment is 2.5. Bold curves represent final, near steady state conditions.
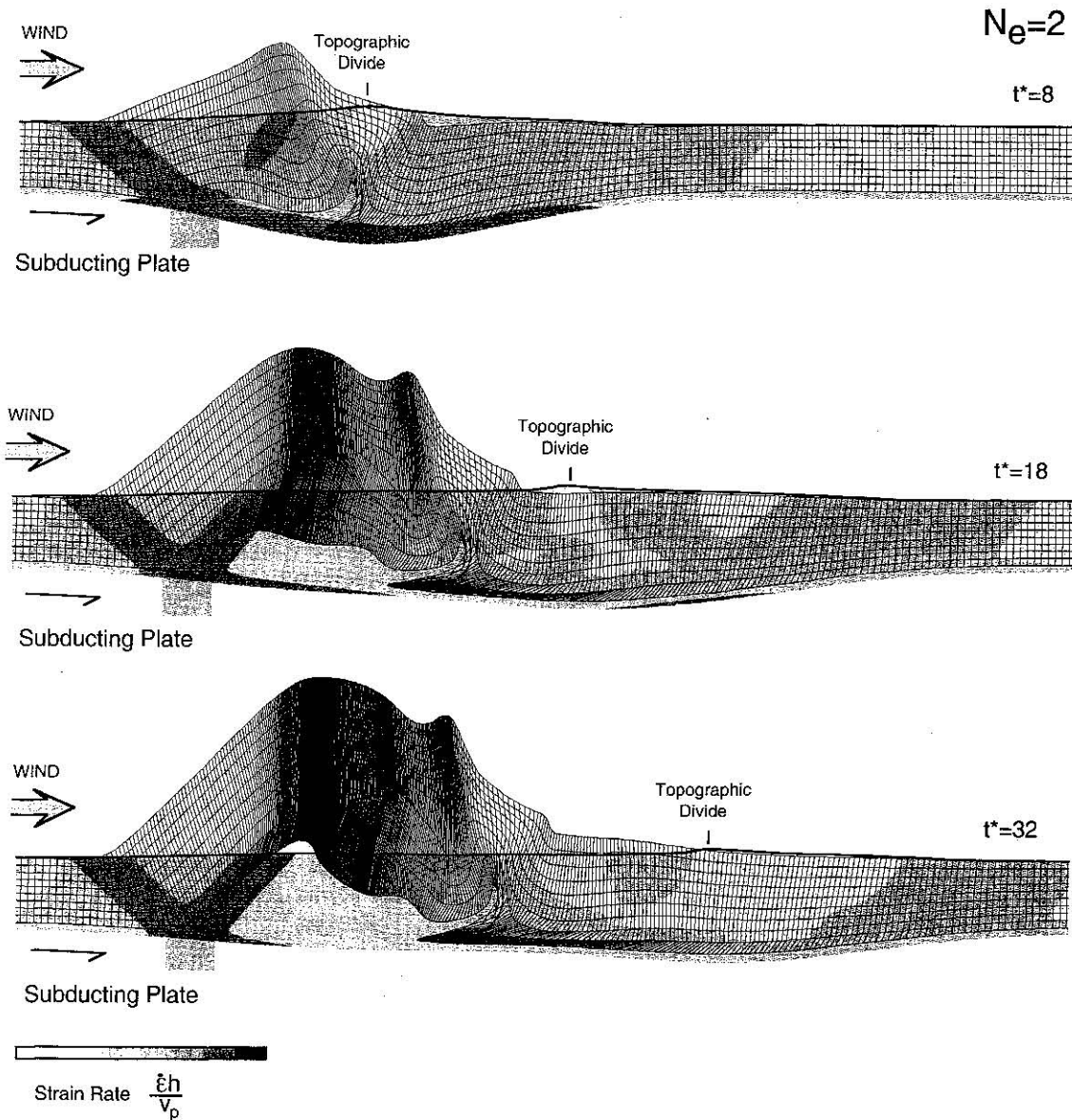
$N_e = 2$

WIND

Topographic Divide

$t^* = 8$

Subducting Plate

WIND

Topographic Divide

$t^* = 18$

Subducting Plate

WIND

Topographic Divide

$t^* = 32$

Subducting Plate

Strain Rate $\dfrac{\dot{\varepsilon}h}{V_p}$

Figure 13. Model with precipitation focused on prowedge. Prowedge is characterized by an erosion number N_e of 2. Retrowedge has no erosion ($N_e = 0$). Results are shown at nondimensional times t^* of 8, 18, and 32. Lower figure is near steady state. See Figure 3 caption for additional model description.

the distribution of exhumation relative to the orogenic deformation.

These characteristic patterns of exhumation are illustrated more clearly by considering orogenic systems in which erosion is more aggressive. With a higher erosional efficiency, reflected in an N_e of 10, and the same asymmetrical precipitation function, we obtain the contrasting models of Figure 15. Regardless of whether erosion is confined to the retrowedge (Figure 15a) or the prowedge (Figure 15b), the exhumation pattern remains the same, with a gradual increase in exhumed depth from left to right and a well-defined exhumation front at the far right of the exhumed region. This sharp front is associated with a distinct shear zone in each model marked by high strain rates. Although the exhumation patterns are similar, the position within the orogen is very different. The model with retrowedge erosion (Figure 15a) has exhumation focused at low elevation at the retrodeformation front, whereas

the maximum exhumation in the prowedge erosion model occurs at high elevation in the orogen interior, just below the topographic divide. As in the previous prowedge erosion model (Figure 13), the focusing of erosion on the prowedge reduces the accretionary growth of the retrowedge and strain rates and surface uplift in the retrowedge decrease to near zero.

Topography also shows the effects of a high erosion rate with significantly subdued steady state topography, which is reached quickly ($t^* = 5$). More important, the high incision rates have allowed the eroding surfaces to incise back into the orogen in the wind direction. This is evident in Figure 15a, where the topographic divide is offset from S, the plate detachment point, in the direction opposite of the tectonic flux. In this case, the erosional incision is more important to the topographic form than the horizontal motion due to the convergence. However, it should be kept in mind that individual material points in this system continue to move left
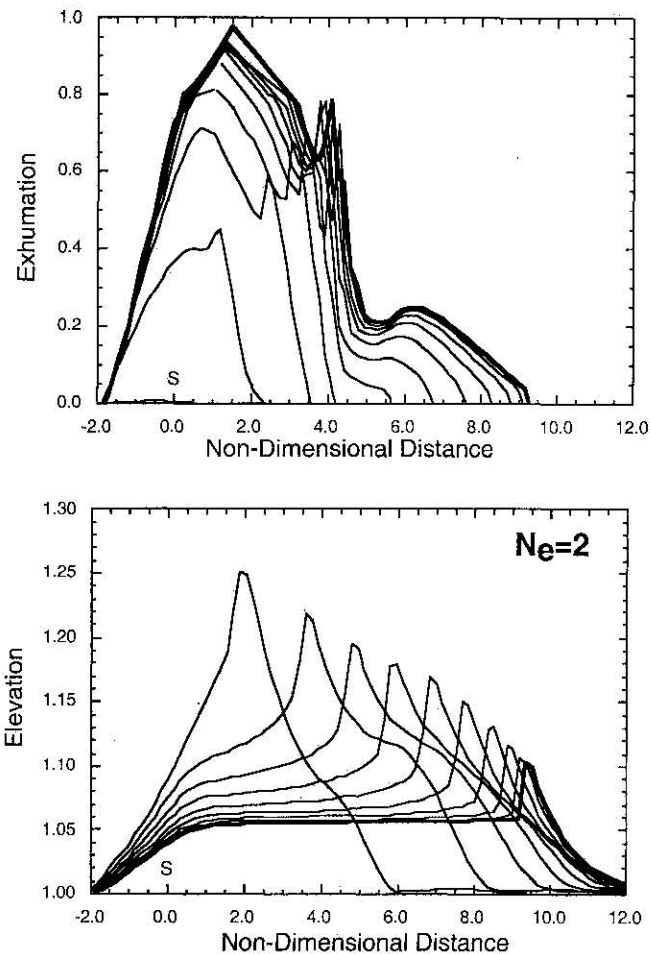
Figure 14. Nondimensional exhumation and elevation as a function of nondimensional time and distance for the model shown in Figure 13. Nondimensional time increment is 4. Bold curves represent final, near steady state conditions.

to right; the upper surface including the topographical divide is an Eulerian surface which moves independently of the material passing through it.

3.3 Discussion of Models

These models provide some valuable insights into the interaction between erosion and deformation in orogenic belts. First, the existence of a steady state in which tectonic accretion and uplift are balanced by erosion is intuitive and is illustrated by these models. The importance of the characteristic scaling number N_e representing the relative efficiency of the erosion system is also demonstrated by these models. Although the specific definition of N_e and the specific results obtained are model dependent, any system with elevation, slope, or relief dependent erosion rates will have similar behavior. The models make specific predictions of topographic cross-sectional form of convergent orogens. These are less likely to be robust. The use of a one-dimensional surface process model is limited in that it restricts analysis to the streambed profile and neglects the independent form of the interfluves. The average elevation across a mountain belt will not be equivalent to the average longitudinal profile of the transverse rivers, and since gravitational stresses in the

mechanical system are a function of the average elevation, this is clearly a limitation of this modeling approach. Addressing this problem would require the use of a 2-D surface process model [*Kooi and Beaumont*, 1996; *Beaumont et al.*, 1999a], a development that would add considerably to the complexity of the model. The model assumptions can be justified in that, first, the erosional fluxes will not be significantly different with a 2-D surface process model, provided the system is near steady state [*Kooi and Beaumont*, 1996] and second, many features of the topography, such as the large-scale asymmetry, are controlled by the mechanical processes. However, the elevation profiles generated by these models should be regarded as approximate and do not resolve the fluvial profile from the average topographic profile.

The exhumation derived from these models does not suffer from such severe limitations. The observed asymmetric exhumation pattern characterized by a sharp exhumation front on the retroside of the system is a function of the subduction polarity. The exhumation pattern is the direct result of the two-dimensionality of the tectonic velocity field and reflects the fact that mass is accreted into the orogen from the subducting plate. For settings in which this orogenic model is applicable [*Willett et al.*, 1993; *Beaumont and Quinlan*, 1994; *Willett and Beaumont*, 1994, *Beaumont et al.*, 1996b], this exhumation pattern becomes a primary characteristic of the kinematic asymmetry of the orogenic process. Surface processes modify the spatial extent of the exhumation and its position relative to topography and deformation but do not alter the overall asymmetry of this pattern. Thus, while effects such as orography and erosional efficiency have notable, predictable effects, the mechanical system still dominates the orogen structure and patterns of exhumation.

4. Natural Systems

Although many first-order characteristics of an orogenic system are determined by tectonic processes, the effects of orographically controlled precipitation are also important to observed uplift and exhumation. This is demonstrated by looking at two modern orogenic systems, the Southern Alps of New Zealand and the Olympic Mountains of the northwest United States, and interpreting these systems in terms of the processes illustrated in the first half of this paper. These orogens were selected for a number of characteristics. First, each is an active tectonic system with high rates of convergence, accretion and uplift. Second, each has a strong orographic climate system with high precipitation and erosion rates linked to the increased elevation. Third, each has been studied extensively so that deformation, structure, metamorphism and degree of exhumation are reasonably well known. Fourth, these two mountain belts provide contrasting examples of orographically enhanced precipitation relative to the polarity of subduction. As such, differences between the orogens come close to isolating the effects of this primary erosion parameter in the same manner that the models in the previous section did.

It should be noted that no attempt will be made to model these orogenic systems in detail. The most robust characteristics of the models are, first, the spatial patterns of exhumation, and, second, the large-scale asymmetry of the resultant topography. These characteristics have a fundamental dependence on tectonic and climatic parameters, and it is these
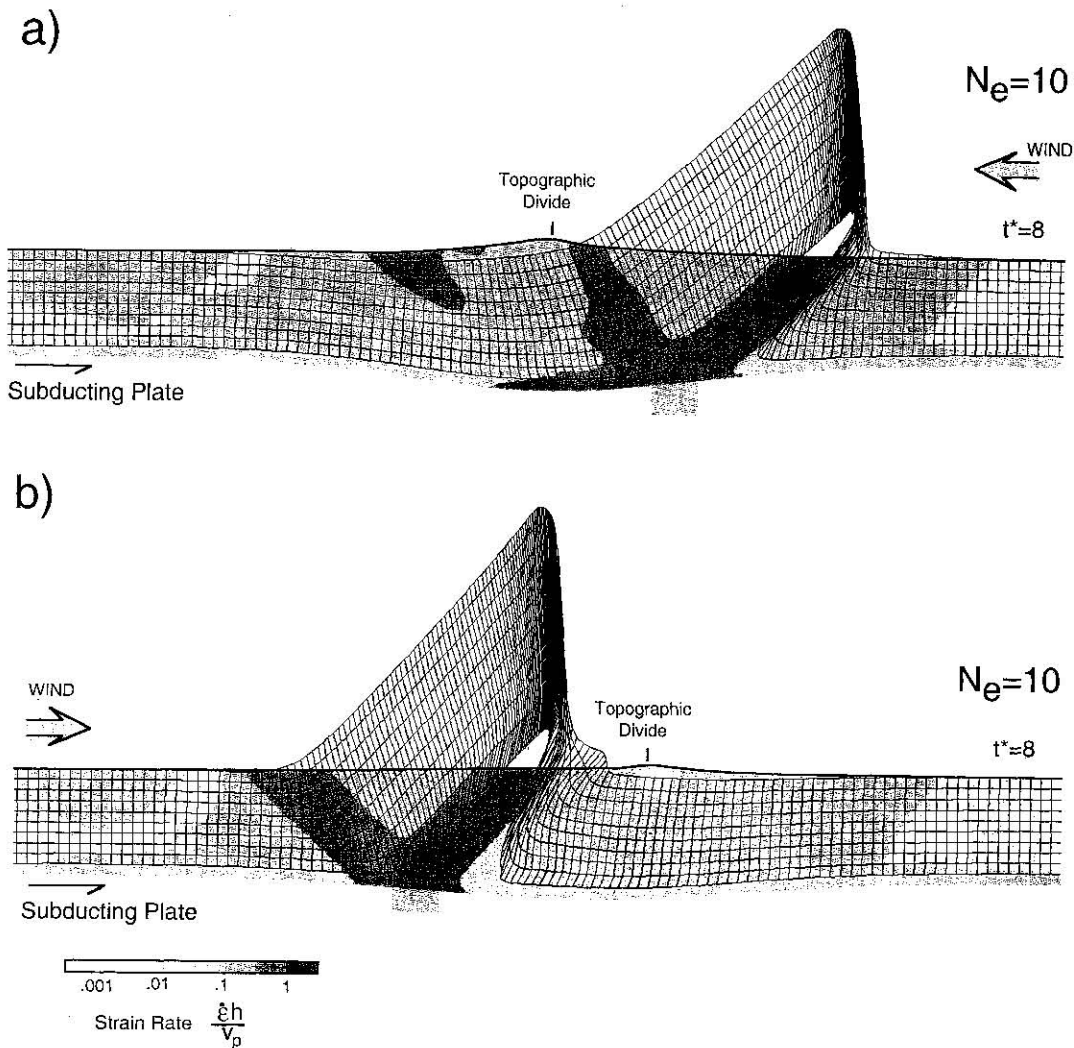
a)

$N_e=10$

WIND

$t^*=8$

Topographic
Divide

Subducting Plate

b)

WIND

$N_e=10$

Topographic
Divide

$t^*=8$

Subducting Plate

.001   .01   .1   1

Strain Rate $\dfrac{\dot{\varepsilon}h}{V_p}$

Figure 15. Model with orographic focusing of precipitation at high erosion number ($N_e=10$): (a) precipitation and erosion focused on retrowedge, and (b) precipitation and erosion focused on prowedge. Results are shown at nondimensional time t^* of 8 which is at steady state. Note similar patterns of exhumation but offset relative to topography. See Figure 3 caption for additional model description.

characteristics and parametric relationships that will be investigated in the latter half of this paper.

4.1 The Southern Alps of New Zealand

4.1.1 Background and geological setting. The Southern Alps of New Zealand have often been used as an example of a young, small collisional orogen with high erosion rates [*Walcott*, 1978; 1998; *Adams*, 1980; *Whitehouse*, 1987; *Kamp et al.*, 1989; *Koons*, 1989; *Norris et al.*, 1990; *Tippet and Kamp*, 1993; *Beaumont et al.*, 1996b; *Batt and Braun*, 1997]. Several factors make this a good example of deformational and erosional processes including the youth of the system, the lack of a long subduction history prior to convergence, and the extremely wet climate that results from the unidirectional moisture flow off the Tasman Sea.

The Southern Alps lie just east of the Alpine fault which marks the boundary between the Australian and Pacific Plates (Figure 16). The Alpine fault is primarily a transform fault that connects the west dipping Hikurangi subduction zone in the

north to the east dipping Puysegur subduction zone to the south. Prior to about 10 Ma, the Alpine fault accommodated pure strike-slip motion, but following a change in the relative plate motions at about anomaly 5 (9.8 Ma), the plate boundary became obliquely convergent [*Stock and Molnar*, 1982]. Currently, the Alpine fault must accommodate approximately 11 mm/yr of convergence in addition to about 38 mm/yr of transcurrent motion [*Norris et al.*, 1990]. The consequence of this relative convergence is crustal shortening, thickening, and the formation of the Southern Alps.

Measured displacements and slip rates across the Alpine fault are systematically less than the relative plate motion [*Walcott*, 1978, 1984; *Cooper and Norris*, 1994] indicating that some fraction of the relative motion is taken up as distributed strain across the Southern Alps. This is evident in surface uplift, with rates in the Southern Alps estimated to be as high as 10 mm/yr and the highest surface uplift and exhumation rates observed along the western mountain front a few kilometers east of the Alpine fault [*Wellman*, 1979; *Walcott*, 1984; *Tippet and Kamp*, 1993].
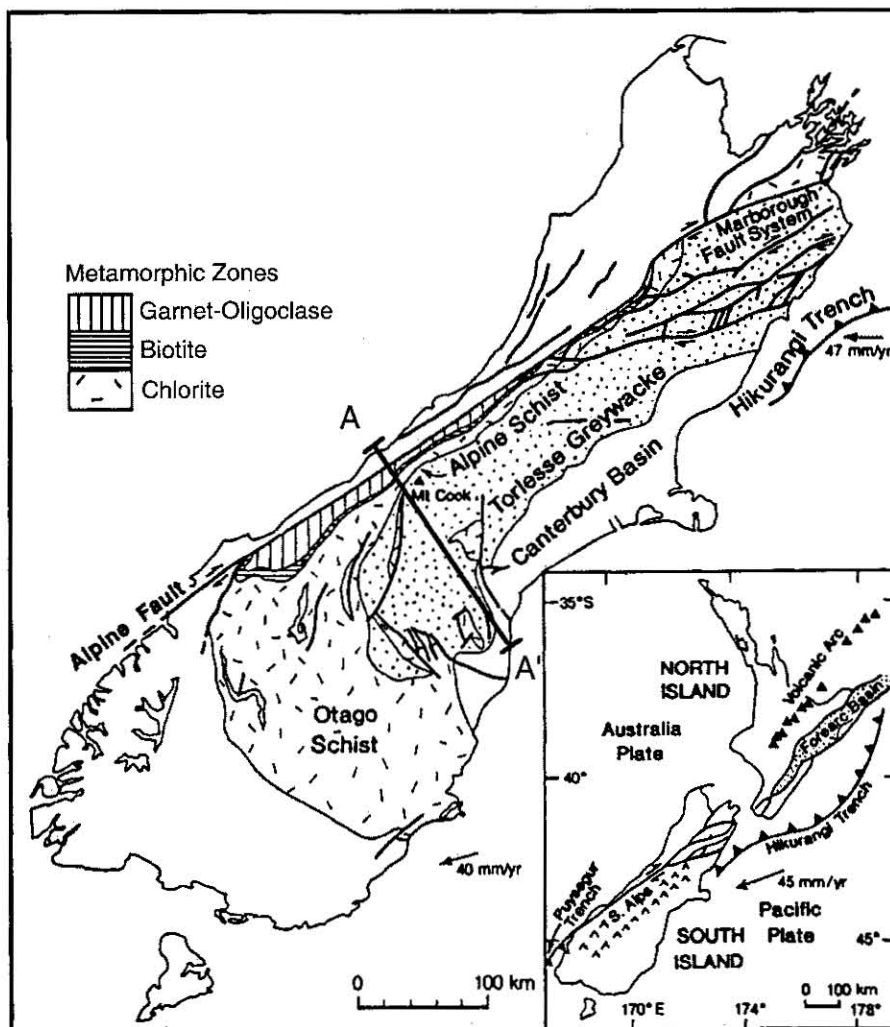
Figure 16. Plate boundary setting of New Zealand (inset) and general geology of the South Island. The Southern Alps lie directly east of the Alpine fault. Metamorphic zones indicating Cenozoic exhumation are also shown. Figure modified from *Beaumont et al.* [1996a].

How the shortening and crustal thickening are accommodated with depth is more difficult to ascertain. Gravity across South Island shows a large negative anomaly [*Reilly and Whitford*, 1979] suggesting the formation of a crustal root, although this inferred root is centered to the east of the range crest. Although there is no seismic evidence for subduction or mantle subduction beneath the Southern Alps, the kinematic pattern is consistent with middle to lower crustal detachment of the Pacific plate with down-to-the west subduction, and the orogen has been interpreted in terms of this model [*Wellman*, 1979, *Norris et al.*, 1990; *Koons*, 1989; *Beaumont et al.*, 1996b] (Figure 18b). This model leads to shortening and thickening of the crust by accretion of Pacific plate material.

4.1.2 Exhumation rates. High Late Cenozoic exhumation rates are observed in the Southern Alps based on thermochronometric data and metamorphism. Greywackes of the Permo-Triassic Torlesse terrane comprise most of the Southern Alps and serve as the protolith for the Otago schist and the Alpine schist (Figure 16) which crop out in the south and west of the Southern Alps. These metamorphic units exhibit increasingly higher grades of metamorphism from the southeast to northwest. The Torlesse terrane experienced Jurassic metamorphism of pumpellyite-actinolite grade, and the Otago schist exhibits Mesozoic metamorphism up to chlorite greenschist facies [*Adams and Gabites*, 1985], but all units exhibit Late Cenozoic metamorphism and exhumation. The Alpine schist is exposed in a narrow belt just east of the Alpine fault and exhibits the highest grade rocks in the Southern Alps with oligoclase and garnet zone amphibolite facies present (Figure 16) [*Tippet and Kamp*, 1993].

Thermochronometric data indicate a pattern of increasing grade and depth of exhumation toward the Alpine fault from the southeast. Apatite and zircon fission track ages decrease systematically from the southeast towards the Alpine fault [*Kamp et al.*, 1989; *Tippet and Kamp*, 1993]. The youngest zircon ages obtained from near the Alpine fault are less than 7 Ma and were interpreted by *Tippet and Kamp* [1993] as reset ages representing cooling due to exhumation from a maximum depth of over 20 km and at rates of up to 10 mm/yr. Other thermochronometers such as K-Ar [*Adams and Gabites*, 1985; *Batt et al.*, 1999] indicate similar patterns of Late Cenozoic

exhumation with high rates close to the Alpine fault. The zones of complete annealing for zircon and apatite are shown in Figure 18b.

4.1.3 Topography and orographically enhanced precipitation. The high rates of exhumation are due in large part to the strong orographic forcing of precipitation by the high topography of the Southern Alps which forms a barrier to moist air flowing eastward from the Tasman Sea. Although the Southern Alps are not extremely high, with an average divide elevation of around 2 km, this is sufficient to produce precipitation that can locally exceed 10 m annually (Figure 17). The precipitation is strongly asymmetric with much of the west coast receiving annual precipitation in excess of 5 m. In contrast, most of the east side of the range receives under 2 m annually (Figure 17).

The geomorphology of the Southern Alps reflects these climatic conditions. The west side of the range is characterized by transverse rivers with steep gradients and high discharge rates separated by steep interfluves [*Adams*, 1980; *Whitehouse*, 1987; *Koons*, 1989] (Fig 18). Erosional processes on the wet, western side of the range are dominated by the fluvial valley lowering and mass wasting off these interfluves. Sediment discharge from the rivers is sufficient to account for the 5 to 10 mm/yr estimated exhumation rates [*Griffiths*, 1979; *Hovius et al.*, 1997; *Tippet and Hovius*, 1999]. The longitudinal profiles of these rivers are remarkably uniform and show the characteristic concave-up shape representative of bedrock incision processes [*Hovius*, 1995].
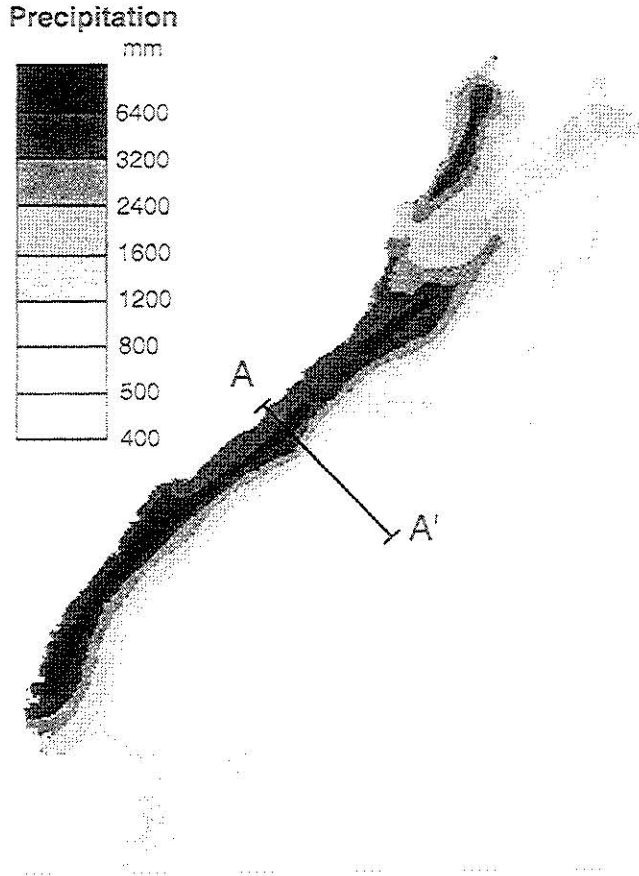
Precipitation
mm

Figure 17. Mean annual precipitation for the South Island of New Zealand.

On the dryer, eastern side of the range, relief is more subdued, and rivers are more strongly influenced by local rock type and geological structure [*Whitehouse*, 1987]. Rivers do not flow perpendicular to the mountain belt; they exhibit a fanning drainage pattern with more southerly rivers flowing more toward the south. The cross-sectional form of the mountain belt is highly asymmetric with much longer, and lower slope rivers flowing to the east and southeast (Figure 18a).

4.1.4 Interpretation and model. The Southern Alps provide a valuable example of the interaction of tectonic and erosional processes for a number of reasons. First, the transition from transverse to convergent motion is simpler than the more common subduction to collision transition in that there is not a highly deformed subduction complex present in the orogenic belt. Second, the high precipitation and erosion rates on the west coast support the possibility that the system is in steady state. Third, the climate system in South Island is highly asymmetrical with distinct wet and dry sides to the mountain belt. In terms of the models of the first section, this represents an example of a wet retrowedge with a large erosion number, N_e.

The pertinent observations of topography, exhumation and precipitation are summarized for a characteristic profile in Figure 18a, with the tectonic interpretation shown in Figure 18b. The exhumation is based on the estimate of *Tippet and Kamp* [1993], which is inferred from interpretation of zircon and apatite fission track data (Figure 18b) and is consistent with other measures of exhumation in showing the deepest levels of exhumation on the western slopes. Precipitation is also highest on the western slopes. These patterns are comparable to the numerical models shown in Figs. 11 and 15a, both of which include erosion focused on the retrowedge of an orogen. Observations from New Zealand (Figure 18a) and these models (Figs. 11 and 15a) are consistent in showing maximum exhumation near the retromountain front, and the Alpine fault can be interpreted as representing an exhumation front as in these models (Figure 18b). Topography in the models of Figs 11 and 15a shows a contrasting sense of asymmetry with the New Zealand data comparable to Figure 11 rather than Figure 15a, a point that is discussed below.

The earlier models that included asymmetric precipitation were end-member models in that the orographic effect was taken as completely effective and there was no precipitation or erosion on leeward slopes. This is clearly not the case in New Zealand, so a more appropriate model is shown in Figure 19. In this model the precipitation rate on the windward side is taken as 3 times larger than on the leeward side resulting in an erosion number of 1.2 for the retrowedge and 0.4 for the leeward, prowedge. Note that the figure has been constructed with the polarity of subduction reversed relative to earlier models to make it consistent with Figure 18b. The resulting elevation and exhumation are shown in detail above the model strain and strain rate fields. The general features of the New Zealand observations are simulated reasonably well by this model. The locus of exhumation on the windward mountain slope as well as the asymmetry of the exhumation pattern are fundamental features of the model and consistent with the New Zealand observations. The model elevation shows the same asymmetry with steeper slopes on the windward, retrowedge, although the asymmetry is not as pronounced as in the observed topography. This is the same result as obtained by *Beaumont et al.* [1996b] who demonstrated that uplift and excess topography could only be focused against the Alpine
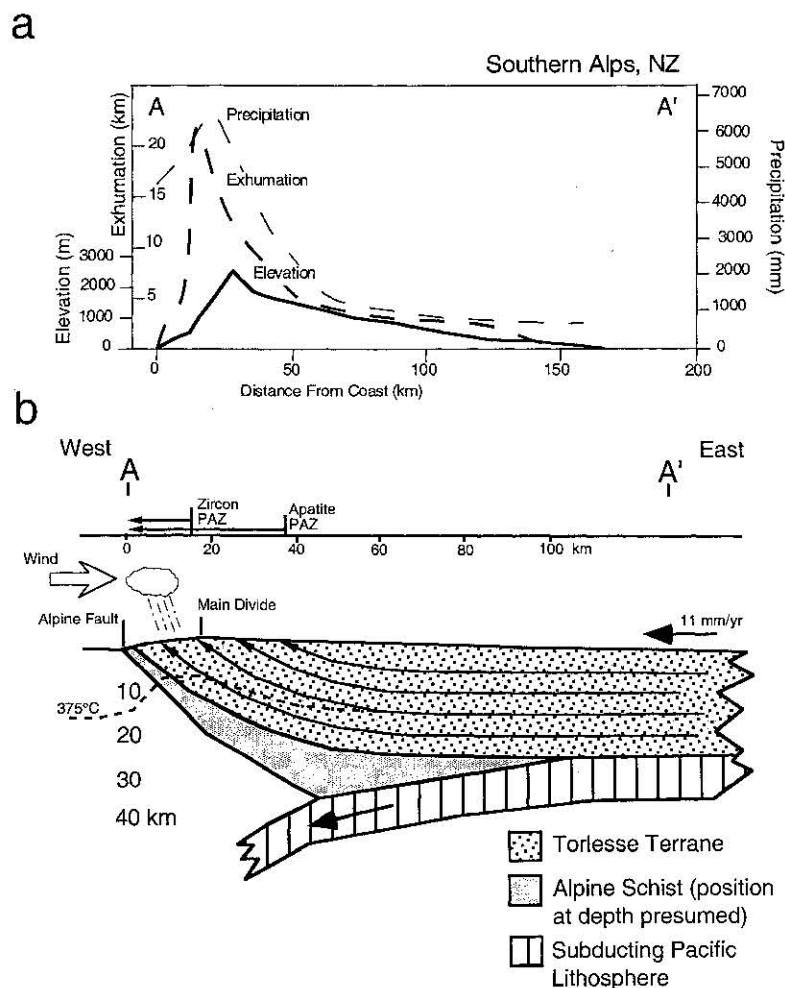
Figure 18. (a) Average elevation, exhumation, and precipitation on transect of Southern Alps. Location of transect is given in Figures 16 and 17. Estimate of exhumation is from *Tippet and Kamp* [1993]. (b) Subduction model for the Southern Alps. Base of the zircon and apatite partial annealing zones indicated above section.

fault to the degree observed if the fault is significantly weaker than the surrounding material, a feature not included in this model.

The topographic asymmetry of the Southern Alps is an important characteristic. Comparison of the models in Figs. 11, 15a and 19 show that the asymmetry of the topographic profile is reversed at high N_e. More powerful rivers on the wet, windward side of the range tend to incise back into the range, decrease river gradients, and eventually reverse the asymmetry of the topography. The fact that the Southern Alps are steeper on the west suggests that the characteristic erosion number is not high and tectonic convergence is still dominating the topography at the largest scale.

4.2 The Olympic Mountains of Washington State

4.2.1 Background and tectonic setting. The Olympic mountains represent an anomalous segment of the forearc high of the Cascadia subduction zone (Figure 20). The forearc high consists of a series of mountain ranges from the Klamaths of northern California to the Insular Range of Vancouver Island. It is a structural and topographic feature that separates the forearc lows of the Willamette Valley, Puget Sound and Georgia Strait

from the offshore accretionary complex and perched offshore basins. The Olympics are anomalous in that, in contrast to the rest of the forearc, the deep levels of the accretionary complex have been exhumed and exposed, thereby providing an opportunity to compare long-term exhumation rates with modern erosion rates and climate. Elsewhere along the continental margin, the forearc sediments are underlain by laterally extensive Eocene basalt (Crescent formation and correlative units), which along with associated sedimentary units, are referred to as the Peripheral rocks [*Tabor and Cady*, 1978a]. In the Olympics the Peripheral rocks have been folded upward and the core of this structure has been eroded to expose the underlying accreted sediments (Figure 20). The formation of this structure has been attributed to the shallower depth to the Juan de Fuca slab beneath the Olympic Peninsula [*Brandon and Calderwood*, 1990]. The Olympic Peninsula became subaerially exposed in the late Miocene [*Brandon and Calderwood*, 1990], significantly earlier than the surrounding regions, and thereby leading to a greater degree of erosion. Although the Olympics have not formed in response to collision between two continental masses as in the Southern Alps of New Zealand, they still represent an orogen formed by
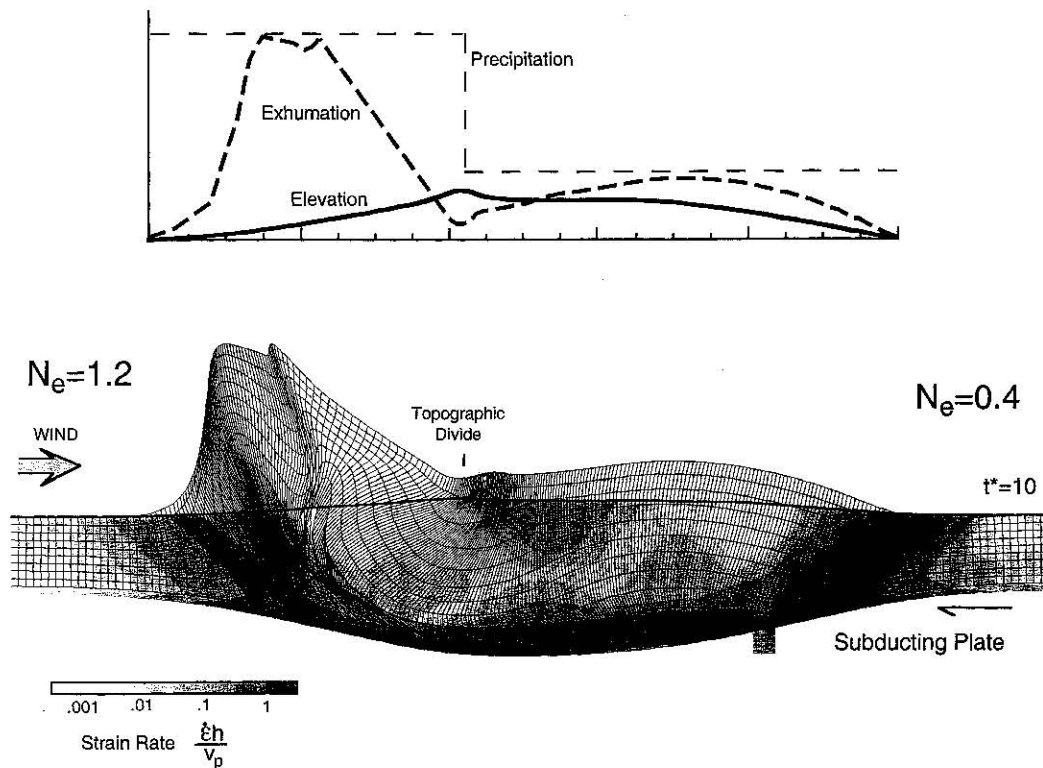
Figure 19. Model with orographic focusing of precipitation such that the retrowedge is characterized by an erosion number N_e of 1.2 and the prowedge by an N_e of 0.4, the approximate ratio of precipitation rate in the Southern Alps of New Zealand. Applied precipitation, predicted elevation, and predicted exhumation for the model are shown above the domain. Note that the polarity of the figure has been reversed relative to models above so that subduction is down to the left to correspond to the New Zealand transect in Figure 18. See Figure 3 caption for additional model description.

convergence and accretion of continental material. In this case the accreted material is sediment derived from the Cordillera of North America and deposited in the trench and offshore basins on the Juan de Fuca plate [*Brandon and Vance*, 1992]. This sediment is accreted either into the front of the accretionary wedge or by landward underplating of the wedge (Figure 22b), but the result is still subduction-driven accretion and deformation with a kinematic pattern consistent with the models of the first section of this paper.

4.2.2 Exhumation patterns and rates. Exhumation of the core rocks of the Olympics has been quantitatively demonstrated by the identification of metamorphic index minerals [*Tabor and Cady*, 1978a, b] and, with greater precision, by fission track studies [*Brandon and Vance*, 1992; *Brandon et al.*, 1998]. *Tabor and Cady* [1978b] identified metamorphic zones reflecting increasing grade from west to east based on the presence of laumonite, prehnite+pumpellyite, pumpellyite, and epidote+chlorite (Figure 20). However, *Brandon and Calderwood* [1990] argue that epidote in the eastmost zone is detrital rather than metamorphic, and they also noted the presence of lawsonite in both the pumpellyite and prehnite+pumpellyite zones. Based on these assemblages, they argued that the maximum pressures and temperatures are exhibited by the pumpellyite-bearing rocks in the center of the Olympic core (Figure 20).

This pattern is also consistent with fission track studies of sandstone in the core. *Brandon and Vance* [1992] studied a suite of zircon samples from the Olympic peninsula and found

that a small subset of them exhibited young ages (<15 Ma), suggesting that they had experienced temperatures high enough to reset the ages. These reset ages all came from samples in the Mount Olympus region in the center of the Olympics (inner bold line in Figure 20). As well as delineating the region of maximum uplift, these zircon fission track ages provided an estimate of the erosion rate of about 1 mm/yr [*Brandon and Vance*, 1992]. In a more recent study, *Brandon et al.* [1998] used apatite fission track ages to characterize the lower temperature systematics of the exhumation processes. They found that apatite ages were reset over a much broader area (outer bold line in Figure 20) consistent with exhumation of the entire core but to a lesser degree. Cooling rates derived from these apatite data were the same as those based on the zircon ages, suggesting that exhumation rates have remained constant over at least the last 12 Ma [*Brandon et al.*, 1998]. This supports the premise that the exhumation rates are in steady state, and insofar as erosion rates depend on the topography, the topography must also be in steady state.

The north-south (margin-parallel) extent of the Olympics is not large, calling into question the assumption of two-dimensional plane-strain. Although the topography and the region of metamorphic exposure appear almost radial in form, major structures are continuous along the margin, and there is little evidence of margin parallel deformation. Kinematic indicators within the Olympic core indicate shortening and kinematic motion in the direction of plate motion [*Tabor and*
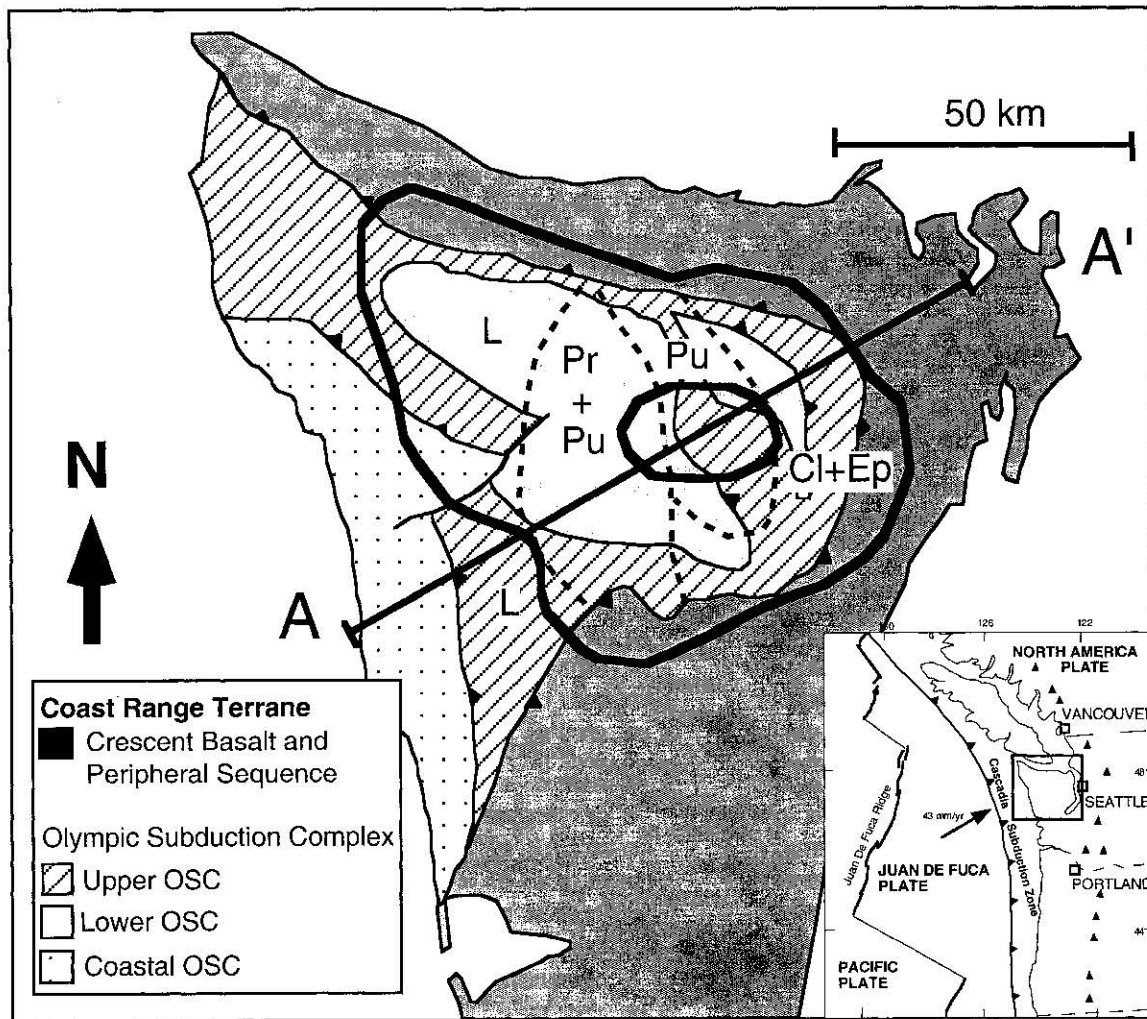
Figure 20. Plate boundary setting of the Olympic Mountains (inset) and general geology [modified from *Brandon et al.*, 1998]. Olympic subduction complex subdivided into upper, lower and coastal units. Bold lines indicate the region of total annealing for apatite (outer domain) and zircon (inner domain) from *Brandon et al.*, [1998]. Dashed lines show metamorphic zones of *Tabor and Cady* [1978a,b] defined by laumonite (L), prehnite-pumpellyite (Pr+Pu), pumpellyite (Pu), and chlorite-epidote (Cl+Ep).

Cady, 1978b; *Brandon et al.*, 1998]. In addition, metamorphic gradients within the core show the most consistent change in the direction of relative plate motion, consistent with a two-dimensional kinematic pattern shown schematically in Figure 22b.

4.2.3 Topography and orography enhanced precipitation. Unroofing of the subduction complex in the Olympics has not been accompanied by extreme surface uplift or high topography. Peak elevations in the Olympics are typically about 2.5 km, and although local relief can be high, this is due, at least in part, to recent glaciation. The limited north-south extent results in an almost radial drainage pattern. However, with the exception of the Elwa River, which runs north to the Straits of Juan de Fuca, the major rivers drain to the west. Rivers all exhibit a concave-up form, although the east flowing rivers are considerably steeper. Rivers on the western slope have different basin lengths, reflecting the changing distance to base level from north to south but, when scaled for basin size, exhibit similar shapes. The east side of the range is much

steeper than the west, as illustrated by the average elevation section of Figure 22a. There is a lithologic factor that could contribute to this asymmetry in that the east-draining rivers cross out of the subduction complex and cross the basaltic peripheral rocks which are likely to be more resistant to erosion. However, most of the area of these drainage basins is in the subduction complex, and although specific topographic features such as Hurricane Ridge are associated with the upturned peripheral rocks, rivers that cross the contact do not show any distinct change in gradient.

Regional climate is also strongly asymmetric, with high precipitation rates observed on the western slopes, where storms approaching from the Pacific first encounter rapid increases in elevation (Figure 21). Precipitation rates can locally exceed 5 m/yr. There is a distinct rainshadow so that the northeast corner of the Olympic peninsula adjacent to Puget Sound receives as little as 80 cm of precipitation annually. Much of the precipitation in the high mountains comes as snow, which feeds the glaciers of the Mount Olympus
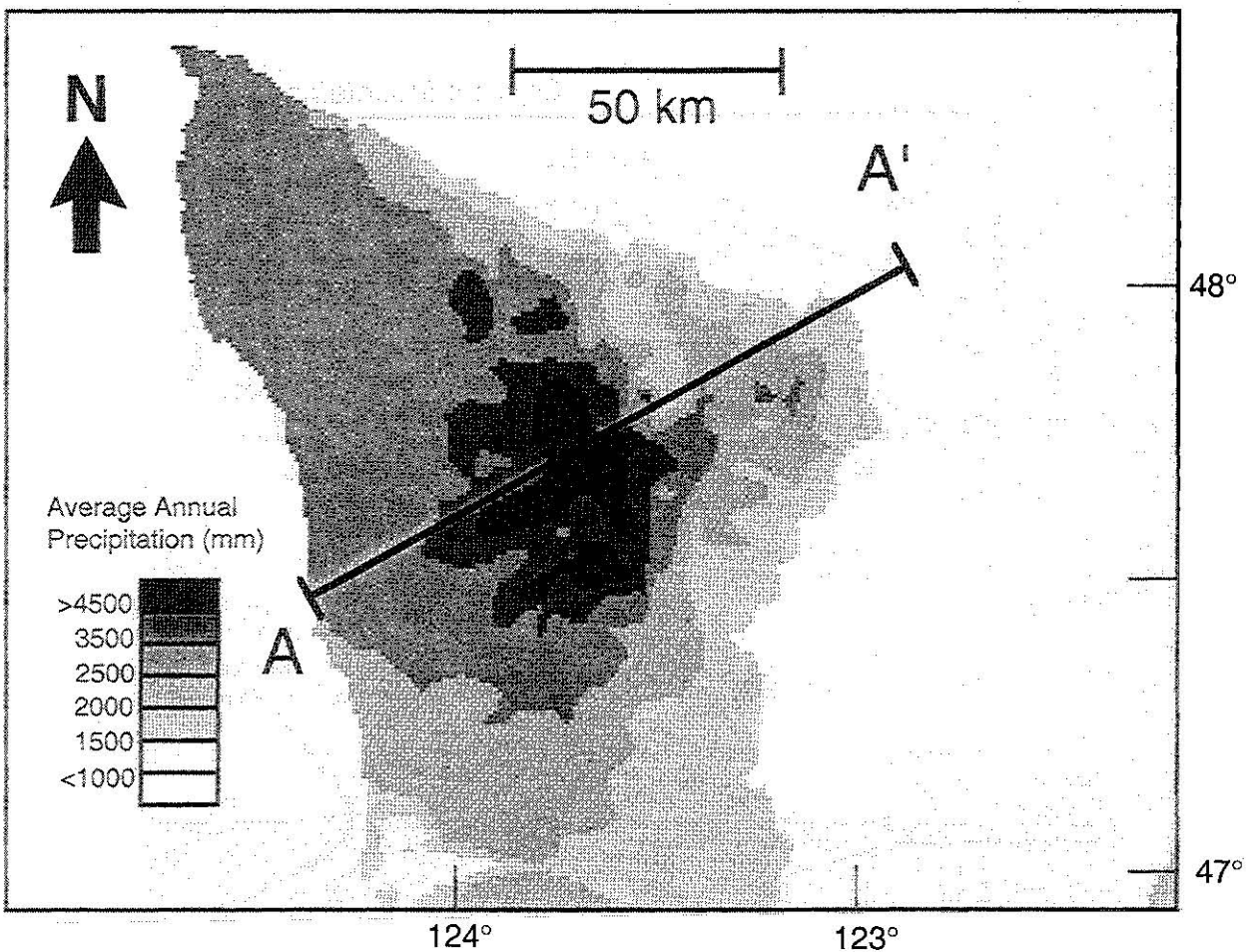
Figure 21. Mean annual precipitation for the Olympic peninsula.
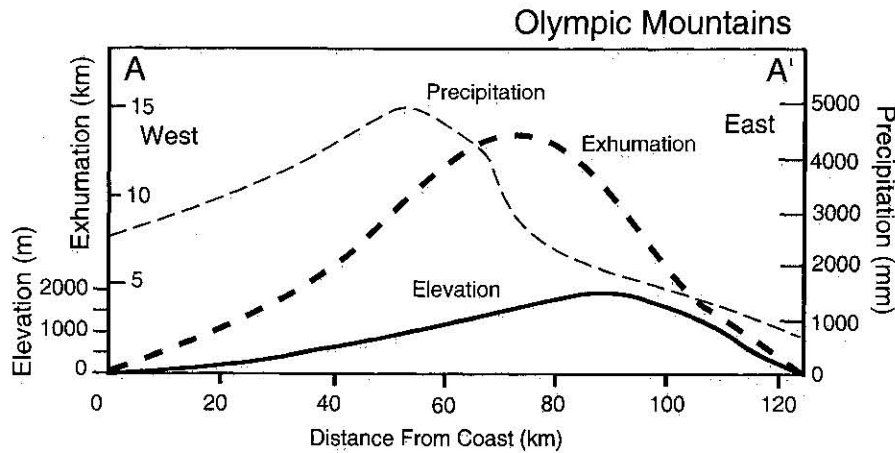
massif region, but these glaciers or the rivers they feed have much more erosive capacity than their east flowing counterparts.

4.2.4 Interpretation and model. The orographic asymmetry of the Olympic mountains is opposite to that of the Southern Alps with respect to the polarity of subduction. The dominant wind direction is in the same direction as motion of the subducting Juan de Fuca plate (Figure 22b) resulting in a wet prowedge similar to the models of Figs. 13 and 15b. The average elevation, exhumation and precipitation for a characteristic transect across the Olympics is shown in Figure 22a. The elevation profile shows steeper slopes to the east, and higher precipitation rates occur on the west facing slopes. The exhumation profile is more difficult to establish and, as in New Zealand, requires some degree of interpretation. In this case, the estimate in Figure 22a is based on the fission track data of *Brandon and Vance* [1992] and *Brandon et al.* [1998] and predicts up to about 14 km of exhumation in a domal pattern centered just west of the average high elevation of the range. Given the asymmetry in precipitation rate, the corresponding numerical models are those shown in Figs 13 and 15b which include erosion only on the prowedge. Those models demonstrate the end-member behavior of the orographic precipitation enhancement, but a more appropriate model is shown in Figure 23. In this model, the precipitation rate on the eastern slopes is half that of the west-facing slopes as an approximation to the observed rates (Figure 22a). Other

parameters in this model remain the same as in the first section of this paper. As was the case for Southern Alps, this model is intended only to show the general behavior, not to fit the data from the Olympics in any detail. Even so, this model shows some important characteristics of the Olympics. First, the asymmetry in the elevation is predicted. As was demonstrated in the modeling section of this paper, the topographic divide migrates in the direction of the subducting plate unless a strongly opposing climate system forces the ridge to migrate in the opposite direction (Figure 15a). Since both climate and subduction are operating to force landward migration of the topographic divide, the observed asymmetry is not diagnostic of the relative importance of these processes, but the asymmetry is consistent with the model.

The modeled pattern of exhumation is also generally consistent with the observations. Both show a broad domal pattern in exhumation. Although the observed exhumation is tighter, more focused in the core of the orogen, the important contrast is between these domal patterns of exhumation and that observed in the Southern Alps and the corresponding models. In the Southern Alps, the exhumation is localized against the Alpine fault with an abrupt exhumation front. No comparable feature is present in the Olympics. The different pattern of exhumation is due to the interaction of the erosional processes and the horizontal motion imposed by the subduction and accretion. The horizontal motion is consistently west to east in the Olympics thereby advecting
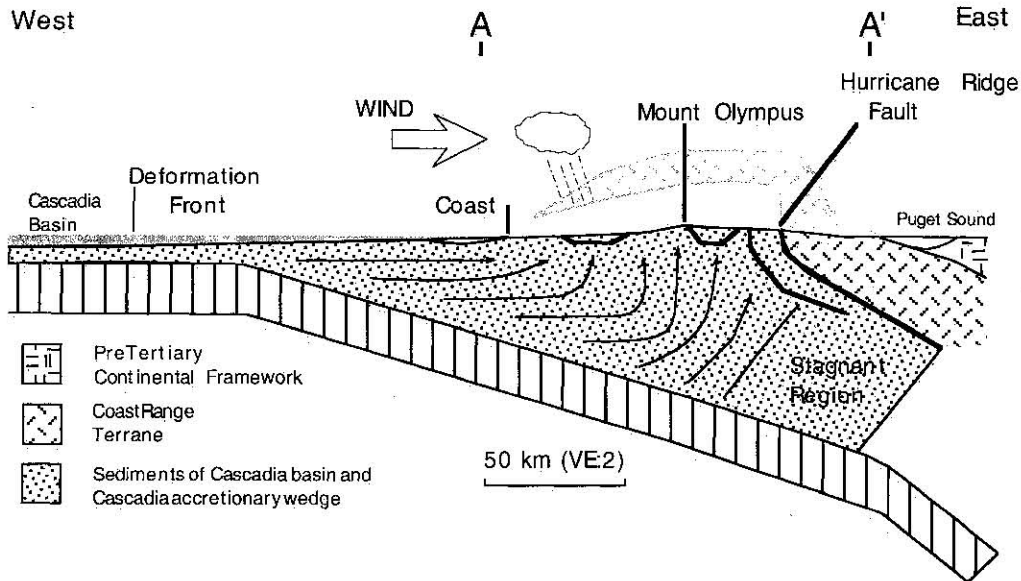
a

Olympic Mountains

b

Figure 22. (a) Average elevation, exhumation and precipitation for a transect of the Olympic Mountains. Location of transect is given in Figures 20 and 21. Exhumation estimate is based on fission track data of *Brandon et al.* [1998] and *Brandon and Vance* [1992]. (b) Accretionary wedge model for the Olympics [modified from *Brandon et al.*, 1998].

topography to the east away from the orographically focused precipitation. This results in a broad region of exhumation with no opportunity for significant exhumation on any individual structure. In addition, the lack of a distinct exhumation front suggests that exhumation is not in steady state; exhumation in the model of Figure 23 is not in steady state although the topography is very near to steady state.

Limitations in this model include the lack of material heterogeneity due to the presence of the peripheral rocks ringing the Olympic peninsula. Mechanical strength in the basalt of these units could tend to decrease the landward (retro-) propagation of deformation and this effect has not been included in the model. In addition, the construction of the accretionary wedge is not modeled very effectively in that, in reality, the accreted sediment layer is no more than a few kilometers thick. The offshore accretionary wedge thickens to about 20 km at the coastline where erosion begins to act on the

system. The model in Figure 23 simulates the deformation of a full thickness crust, thereby ignoring the deformation processes in the offshore accretionary wedge. However, provided the accretionary wedge at the coastline is homogeneous and the later deformation is not dependent on the earlier history, modeling of the ~20 km thick constant-thickness layer will be equivalent to modeling the thickened accretionary wedge.

5. Summary and Conclusions

The coupled deformation-erosion model presented in this paper is used to investigate the important interactions between tectonic deformation, surface uplift, climate, and exhumation. The principal assumptions of this model are, first, that convergent orogens form as the result of a subduction-accretion process and, second, that the erosion process is dominated by a streampower-based fluvial incision process.
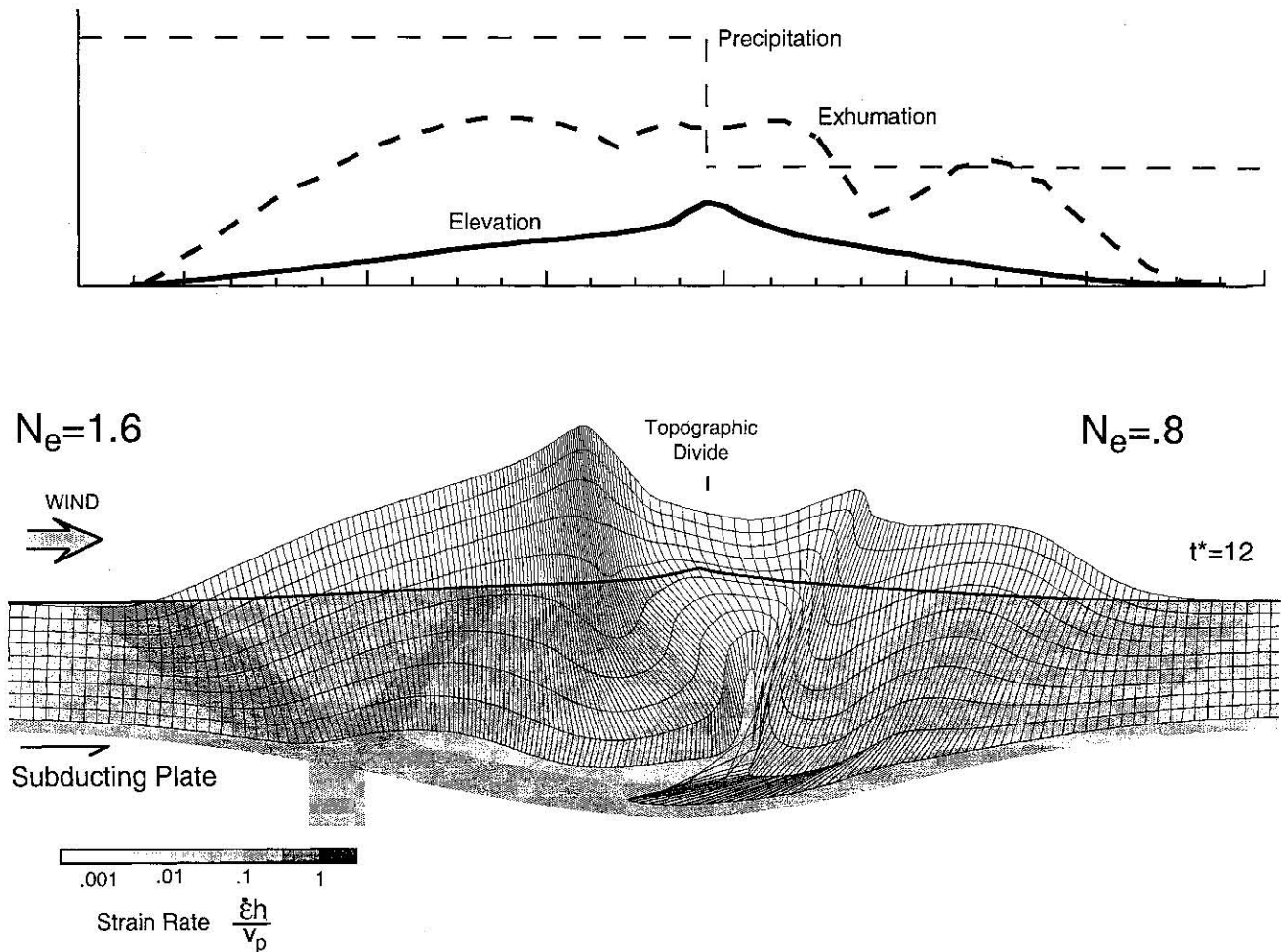
Figure 23. Model with orographic focusing of precipitation such that the prowedge is characterized by an erosion number N_e of 1.6 and the retrowedge by an N_e of 0.8. Applied precipitation, predicted elevation, and predicted exhumation from the model are shown above the domain. See Figure 3 caption for additional model description.

Subject to these assumptions and based on this model, the following conclusions can be made.

1. With positive feedback between surface elevation and erosion rate, the height of an orogen will grow until reaching a steady state. Positive feedback arises from enhanced precipitation, increased average slope, or enlarged drainage basin area, all of which lead to greater stream power and higher rates of fluvial incision. The time to steady state and the final size of the mountain belt are determined by the ratio of convergence velocity to a characteristic erosion rate in the form of a dimensionless "erosion number." A steady state is achieved even with low erosion rates on the leeward side of a mountain belt with uplift rates balanced by horizontal advection rates.

2. The critical topographic profile of a mountain belt formed by a subduction-accretion process is asymmetric in the absence of erosion with steeper slopes on the retrowedge verging toward the overriding plate and lower slopes on the prowedge verging toward the subducting plate. Erosion driven by symmetric precipitation and fluvial incision will sharpen this topographic form but will not change the asymmetry.

3. Patterns of exhumation are distinctly asymmetric reflecting the polarity of the subduction. The deepest levels of

exhumation are always opposite the subducting plate. In a steady state system this results in a well-defined exhumation front facing the stable overriding plate with a more gradual decrease in the level of exhumation toward the subducting plate. Differing climatic conditions can broaden this characteristic pattern or offset it relative to the surface uplift, but the asymmetry of the pattern is consistent.

4. The existence of a dominant wind direction imposes a second asymmetry on the system. Enhanced precipitation and erosion rate can occur on either side of an orogen with significantly different effects. If erosion is enhanced on the retrowedge above the overriding plate, exhumation is increasingly localized, and a well-developed exhumation front develops. At steady state the erosional mass flux from the retrowedge equals the accreted mass flux, and topography of the prowedge is maintained by the balance between structural thickening and horizontal advection of mass. At high erosion number, fluvial incision dominates over uplift, the topographic divide migrates in the direction opposite the tectonic flux, and the topographic asymmetry of the orogen is reversed. If erosion is enhanced on the prowedge, the exhumation pattern is broadened as convergence advects structure and topography away from the zone of enhanced erosion. The region of

maximum exhumation is found in the orogen interior. At high erosion number and steady state conditions, the retrowedge is mechanically detached from the tectonic mass transport system and becomes inactive.

5. Natural examples of orogens that exhibit primary features of these coupled models exist, demonstrating that the important effects of these models have geological relevance. The Southern Alps of New Zealand and the Olympic Mountains of Washington State were selected to show the end-member behavior of systems with asymmetric climatic effects. Although models can be fit to observations from these orogens and calibrated to estimate erosion parameters, the principle value of the exercise is in comparison of the spatial patterns of topography and exhumation of rocks presently at the surface.

6. The Southern Alps of New Zealand provide an example of enhanced retrowedge erosion. Average annual precipitation rate decreases by a factor of about 3 across the range divide. Exhumation is strongly localized at the Alpine fault and represents approximately 10 times the maximum present elevation, consistent with the exhumation pattern characteristic of the models with enhanced retrowedge erosion. The elevation profile of the southern Alps is asymmetric with the steeper slopes on the wet, retrowedge, suggesting that the erosion number is still low enough that tectonic advection dominates over fluvial incision in determining topography at the largest scale.

7. A complementary example of enhanced erosion on the prowedge of an orogen is provided by the Olympic Mountains of Washington State. Erosion of the forearc high of the Cascadia accretionary wedge is orographically enhanced by high precipitation rates on the western slopes. Exhumation estimated by fission track studies shows a broad, domal pattern with maximum values of about 14 km in the center of the orogen, consistent with a model including enhanced prowedge erosion. Topography is not diagnostic in this case but is strongly asymmetric, with steeper slopes on the dryer, landwardfacing retrowedge.

References

Adams, C.J., and J.E. Gabites, Age of metamorphism and uplift in the Haast Schist Group at Haast Pass, Lake Wanaka, and Lake Hawea, South Island, New Zealand, *N. Z. J. Geol. Geophys.*, *28*, 85-96, 1985.

Adams, J., Contemporary uplift and erosion of the Southern Alps, New Zealand, *Geol. Soc. Am. Bull. Part II, 91*, 1-114, 1980.

Anderson, R.S., Evolution of the Santa Cruz Mountains, California, through tectonic growth and geomorphic decay, *J. Geophys. Res., 99*, 20161-20179, 1994.

Barr, T.D., and F. A. Dahlen, Brittle frictional mountain building, 2, Thermal structure and heat budget, *J. Geophys. Res., 94*, 3923-3947, 1989.

Barr, T.D., F.A. Dahlen, and D.C. McPhail, Brittle frictional mountain building 3. Low-grade metamorphism, *J. Geophys. Res., 96*, 10,319-10,338, 1991.

Barry, R.G., *Mountain Weather and Climate*, 313 pp., Methuen, New York, 1981.

Batt, G.E., and J. Braun, On the thermo-mechanical evolution of compressional orogens, *Geophys. J. Int., 128*, 364-382, 1997.

Batt, G.E., B.P. Kohn, J. Braun, I. McDougall, and T.R. Ireland, New insight into the dynamic development of the Southern Alps, New Zealand, from detailed thermochronological investigation of the Mataketake Range pegmatites, in *Exhumation Processes: Normal Faulting, Ductile Flow and Erosion*, edited by U. Ring, M. Grandon, G. Lister, and S. D. Willett, *Spec. Publ. Geol. Soc. London*, 154, pp. 261-282, 1999.

Beaumont, C., and, G. Quinlan, A geodynamic framework for interpreting crustal-scale seismic-reflectivity patterns in compressional orogens, *Geophys. J. Int., 116*, 754-783, 1994.

Beaumont, C., P. Fullsack, and J. Hamilton, Erosional control of active compressional orogens, in *Thrust Tectonics*, edited by K. R. McClay, pp. 19-31, Chapman and Hall, New York, 1992.

Beaumont, C., S. Ellis, J. Hamilton, and P. Fullsack, Mechanical model for subduction-collision tectonics of Alpine-type compressional orogens, *Geology, 24*, 675-678, 1996a.

Beaumont, C., P.J.J. Kamp, J. Hamilton, and P. Fullsack, The continental collision zone, South Island New Zealand; Comparison of geodynamic models and observations, *J. Geophys.Res., 101*, 3333-3359, 1996b.

Beaumont, C., H. Kooi, and S. D. Willett, Progress in coupled tectonic - Surface Process Models with applications to rifted margins and collisional orogens, in *Geomorphology and Global Tectonics,* edited by M. Summerfield, in press, 1999a.

Beaumont, C., J. A. Munoz, , J. Hamilton, and P. Fullsack, Factors controlling the Alpine evolution of the central Pyrenees inferred from a comparison of observations and geodynamical models, *J. Geophys. Res.*, in press, 1999b.

Bird, P., New finite element techniques for modeling deformation histories of continents with stratified temperature-dependent rheology, *J. Geophys. Res., 94*, 3967-3990, 1989.

Bird, P., Lateral extrusion of lower crust from under high topography, in the isostatic limit, *J. Geophys. Res., 96*, 10,275-10,286, 1991.

Brandon, M.T., and A.R. Calderwood, High-pressure metamorphism and uplift of the Olympic subduction complex, *Geology, 18*, 1252-1255,1990.

Brandon, M.T., and J.A. Vance, New statistical methods for analysis of fission-track grain-age distributions with applications to detrital zircon ages from the Olympic subduction complex, Western Washington State, *Am. J. Sci., 292*, 565-636, 1992.

Brandon, M. T., M. K. Roden-Tice, and J.I. Garver, Late Cenozoic exhumation of the Cascadia accretionary wedge in the Olympic Mountains, NW Washington State, *Geol. Soc. Am. Bull., 110*, 985-1009, 1998.

Braun, J., and C. Beaumont, Three-dimensional numerical experiments of strain partitioning at oblique plate boundaries: Implications for contrasting tectonic styles in the southern Coast Ranges, California, and central South Island, New Zealand, *J. Geophys. Res., 100*, 18059-18074, 1995.

Braun, J., and M. Sambridge, Modelling landscape evolution on geological time scales: A new method based on irregular spatial discretization. *Basin Res., 9*, 27-52, 1997.

Chapple, W.M., Mechanics of thin-skinned fold-and-thrust belts, *Geol. Soc. Am. Bull., 89*, 1189-1198, 1978.

Chase, C.G., Fluvial landsculpting and the fractal dimension of topography, *Geomorphology, 5*, 39-57, 1992.

Cooper, A.F., and R.J. Norris, Anatomy, structural evolution, and slip rate of a plate-boundary thrust: The Alpine Fault at Gaunt Creek, Westland, New Zealand, *Geol. Soc. Am. Bull., 106*, 627-633, 1994.

Dahlen, F.A., Noncohesive critical Coulomb wedges: An exact solution, *J. Geophys. Res., 89*, 10125-10133, 1984.

Dahlen, F.A., Critical taper model of fold-and-thrust belts and accretionary wedges, *Annu. Rev. Earth Planet. Sci., 18*, 55-99, 1990.

Davis, D., J. Suppe, and F.A. Dahlen, Mechanics of fold-and-thrust belts and accretionary wedges, *J. Geophys. Res., 88*, 1153-1172, 1983.

Densmore, A. L., M. A. Ellis, and R.S. Anderson, Landsliding and the evolution of normal-fault-bounded mountains, *J. Geophys. Res., 103*, 15,203-15,219, 1998.

Ellis, S., P. Fullsack, and C. Beaumont, Oblique convergence of the crust driven by basal forcing: Implications for length-scales of deformation and strain partitioning in orogens, *Geophys. J. Int., 120*, 24-44, 1995.

England, P., and D.P. McKenzie, A thin viscous sheet model for continental deformation, *Geophys. J. R. Astron. Soc., 70*, 295-321, 1982.

England, P., G. Houseman, and L. Sonder, Length scales for continental deformation in convergent, divergent and strike-slip environments: Analytical and approximate solutions for a thin viscous sheet model, *J. Geophys. Res., 90*, 4797-4810, 1985.

Fullsack, P., An arbitrary Lagrangian-Eulerian formulation for creeping flows and its application in tectonic models, *Geophys. J. Int., 120*, 1-23, 1995.

Gilbert, G.K., *Report on the Geology of the Henry Mountains*, U.S. Govt. Print. Off., Washington, D.C., 1877.

Griffiths, G.A., High sediment yields from major rivers of the western Southern Alps, New Zealand, *Nature, 282*, 61-63, 1979.

Hovius, N., Macroscale process systems of mountain belt erosion and sediment delivery to basins, Ph.D. thesis, Oxford, England, Univ. of Oxford, 1995.

Hovius, N., C.P. Stark, and P.A. Allen, Sediment flux from a mountain belt derived by landslide mapping, *Geology, 25*, 231-234, 1997.

Howard, A.D., and G. Kerby, Channel changes in badlands, *Geol. Soc. of Am. Bull., 94*, 739-752, 1983.

Jamieson, R.A., and C. Beaumont, Orogeny and metamorphism: A model for deformation and P-T-t paths with applications to the central and southern Appalachians, *Tectonics, 7*, 417-445,1988.

Jamieson, R.A., C. Beaumont, J. Hamilton, and P. Fullsack, Tectonic assembly of inverted metamorphic sequences, *Geology, 24*, 839-842, 1996.

Kamp, P.J.J., P.F. Green, and S. H. White, Fission track analysis reveals character of collisional tectonics in New Zealand, *Tectonics, 8*, 169-195, 1989

Kohlstedt, D. L., B. Evans, and S. J. Mackwell, Strength of the lithosphere: Constraints imposed by laboratory experiments, *J. Geophys. Res., 100*, 17,587-17,602, 1995.

Kooi, H., and C. Beaumont, Escarpment retreat on high-elevation rifted continental margins: Insights derived from a surface-processes model that combines diffusion, reaction and advection, *J. Geophys. Res., 99*, 12,191-12,209, 1994.

Kooi, H., and C. Beaumont, Large-scale geomorphology: Classical concepts reconciled and integrated with contemporary ideas via a surface processes model, *J. Geophys. Res., 1012*, 3361-3386, 1996.

Koons, P.O., The topographic evolution of collisional mountain belts: A numerical look at the Southern Alps, New Zealand, *Am. J. Sci., 289*, 1041-1069, 1989.

Leopold, L.B., M.G. Wolman, and J.P. Miller, *Fluvial Processes in Geomorphology*, Freeman, Cooper, San Francisco, Calif., 1964.

Masek, J.G., B.L. Isacks, T.L. Gubbels, and E.J. Fielding, Erosion and tectonics at the margins of continental plateaus, *J. Geophys. Res., 99*, 13,941-13,956, 1994.

Morris, R. G., H. D. Sinclair, and A. J. Yelland, Exhumation of the Pyrenean orogen: implications for sediment discharge, *Basin Res., in press*, 1999.

Norris, R. J., P.O. Koons, and A. F. Cooper, The obliquely-convergent plate boundary in the South Island of New Zealand: Implications for ancient collision zones, *J. Struct. Geol., 12*, 715-725, 1990.

Reilly, W.I., and C.M. Whitford, Gravity map of New Zealand, 1:1,000,000: Bouguer and isostatic anomalies, South Island, Dep. of Sci. and Ind. Res., Wellington, New Zealand, 1979.

Royden, L., Coupling and decoupling of crust and mantle in convergent orogens: Implications for strain partitioning in the crust, *J. Geophys. Res., 101*, 17,679-17,705, 1996.

Schlunegger, F., and S. D. Willett, Spatial and temporal variations in exhumation of the central Swiss Alps and implications for denudation mechanisms, in *Exhumation Processes: Normal Faulting, Ductile Flow and Erosion*, edited by U. Ring, M. Brandon, G. Lister, and S. D. Willett, *Spec. Publ. Geol. Soc. London*, 154, pp. 157-179, 1999.

Schmid, S.M., O.A. Pfiffner, N. Froitzheim, G. Schönborn, and E. Kissling, Geophysical-geological transect and tectonic evolution of the Swiss-Italian Alps, *Tectonics, 15*, 1036-1064, 1996.

Seidl, M. A., and W. E. Dietrich, The problem of channel erosion into bedrock, *Catena Suppl., 23*, 101-124, 1992.

Seidl, M. A., W. E. Dietrich, and J. W. Kirchner, Longitudinal profile development into bedrock: An analysis of Hawaiian channels, *J. Geol., 102*, 457-474, 1994.

Silver, E.A., and D.L. Reed, Backthrusting in accretionary wedges, *J. Geophys. Res., 93*, 3116-3126, 1988.

Sklar, L., W. E. Dietrich, and A. D. Howard, The influence of sediment supply on river incision into bedrock; a theoretical investigation, *Eos Trans. AGU, 77*(46) Fall Meet. Suppl., 251, 1996.

Slingerland, R., S. D. Willett, and H. Hennessey, A new fluvial bedrock erosion model based on the work-energy principle, *Eos Trans. AGU, 78*(46) Fall Meet. Suppl., 299, 1997.

Stock, J., and P. Molnar, Uncertainties in the relative positions of the Australia, Antarctica, Lord Howe, and Pacific plates since the Late Cretaceous, *J. Geophys. Res., 87*, 4697-4714, 1982.

Stock, J. and D. Montgomery, Geological constraints on bedrock river incision using the stream power law, *J. Geophys. Res., 104*, 4983-4993,1999.

Suppe, J., A retrodeformable cross section of northern Taiwan, *Geol. Soc. China Proc., 23*, 46-55, 1980.

Suppe, J., Mechanics of mountain building and metamorphism in Taiwan, *Mem. Geol. Soc. China, 4*, 67-89, 1981.

Tabor, R.W., and W.M. Cady, The structure of the Olympic Mountains, Washington- Analysis of a subduction zone, *U.S. Geol. Surv. Prof. Pap., 1033*, 38 pp., 1978a.

Tabor, R.W., and W.M. Cady, Geologic map of the Olympic Peninsula, *U.S. Geol. Surv. Map. I-994*, scale 1:125000, 1978b.

Tippett, J.M., and N. Hovius, Geodynamic processes in the Southern Alps, New Zealand, in *Geomorphology and Global Tectonics*, edited by M. Summerfield, John Wiley, in press, 1999.

Tippett, J. M., and P.J.J. Kamp, Fission track analysis of the late Cenozoic vertical kinematics of continental Pacific crust, South Island, New Zealand, *J. Geophys. Res., 98*, 16,119-16,148, 1993.

Tucker, G. E., and R. Slingerland, Erosional dynamics, flexural isostasy, and long-lived escarpments: A numerical modeling study, *J. Geophys. Res., 99*, 12,229-12,243, 1994.

Turcotte, D.L. and G. Schubert, *Geodynamics: Applications of ontinuum Physics to Geological Problems*, 450 pp., John Wiley, New York, 1982.

Walcott, R. I., Present tectonics, and Late Cenozoic evolution of New Zealand, Geophys. *J. R. astron. Soc., 52*, 137-164, 1978.

Walcott, R. I., The kinematics of the plate boundary zone through New Zealand: a comparison of short- and long-term deformations, *Geophys. J. R. astron. Soc., 79*, 613-633, 1984.

Walcott. R. I., Modes of oblique compression: Late Cenozoic tectonics of the South Island of New Zealand, *Rev. Geophys., 36*, 1-26, 1998.

Wang, W.-H., and D. M. Davis, Sandbox model simulation of forearc evolution and non-critical wedges, *J. Geophys. Res., 101*, 11,329-11339, 1996.

Wdowinski, S., and Y. Bock, The evolution of deformation and topography of high elevated plateaus 1. Model, numerical analysis, and general results, *J. Geophy. Res., 99*, 7103-7119, 1994.

Wellman, H.W., An uplift map for the South Island of New Zealand, and a model for uplift of the Southern Alps, in *The Origin of the Southern Alps*, edited by R.I. Walcott and M.M. Cresswell, *Bull. R. Soc. N.Z., 18*, 13-20, 1979.

Whitehouse, I. E., Geomorphology of a compressional plate boundary, Southern Alps, New Zealand, in *International Geomorphology, 1986, part I*, edited by V. Gardiner, pp. 897-924, John Wiley, 1987.

Willett, S. D., Dynamic and kinematic growth and change of a Coulomb wedge, in *Thrust Tectonics*, edited by K. McClay, pp. 19-31, Chapman and Hall, New York, 1992.

Willett, S. D., Rheological dependence of extension in viscous and plastic wedge models of convergent orogens, *Tectonophysics, 305*, 419-435, 1999.

Willett, S. D., and C. Beaumont, Subduction of Asian lithospheric mantle beneath Tibet inferred from models of continental collision, *Nature, 369*, 642-645, 1994.

Willett, S. D., C. Beaumont, and P. Fullsack, Mechanical model for the tectonics of doubly vergent compressional orogens, *Geology, 21*, 371-374, 1993.

S. D. Willett, Department of Geological Sciences, University of Washington, Seattle, WA 98125 (swillett@u.washington.edu)